

TABLE 1  
ABELL 2390 CATALOG

PPP# (a)	$r$ (b)	$g - r$ (c)	$r_p$ (d)	$z$ (e)	S/N (f)	D4000 (g)	$H\delta$ (h)	[O II] (i)	$C$ (j)	$\mu_r$ (k)	Member (l)
101084	17.31	$0.68 \pm 0.05$	0.0	0.2301	14.6	$1.57 \pm 0.03$	$2.0 \pm 0.9$	$-111.1 \pm 5.2$	$0.49 \pm 0.04$	22.6	member
201357	17.40	$0.61 \pm 0.05$	427.9	0.1148	...	...	$0.2 \pm 1.1$	...	$0.69 \pm 0.04$	24.5	field
300560	17.48	$0.46 \pm 0.05$	388.8	0.1700	10.5	$1.63 \pm 0.05$	$7.5 \pm 1.5$	...	$0.49 \pm 0.04$	24.1	field
300495	17.72	$0.75 \pm 0.05$	581.8	0.1785	13.8	$2.16 \pm 0.06$	$-0.1 \pm 0.9$	...	$0.60 \pm 0.02$	24.0	field
100615	17.98	$0.85 \pm 0.05$	189.6	0.2315	14.8	$2.37 \pm 0.06$	$-1.7 \pm 0.8$	...	$0.56 \pm 0.03$	23.4	member
201263	18.04	$0.70 \pm 0.05$	724.0	0.2240	22.0	$2.2 \pm 0.04$	$0.8 \pm 0.8$	...	$0.64 \pm 0.08$	21.8	member
200932	18.08	$0.48 \pm 0.05$	698.4	0.2230	5.6	$2.63 \pm 0.24$	$8.4 \pm 2.3$	...	$0.47 \pm 0.04$	23.6	member
100537	18.18	$0.56 \pm 0.05$	130.9	0.2210	21.6	$1.83 \pm 0.03$	$7.5 \pm 0.7$	...	...	...	member
101818	18.22	$0.42 \pm 0.05$	176.9	0.2168	10.4	$1.7 \pm 0.05$	$4.7 \pm 1.4$	...	$0.42 \pm 0.02$	24.3	member
200561	18.24	$0.50 \pm 0.05$	516.9	0.1793	8.1	$2.35 \pm 0.14$	$2.6 \pm 1.6$	...	$0.58 \pm 0.08$	24.5	field
131855	18.40	$0.61 \pm 0.05$	302.6	0.1080	...	...	$2.8 \pm 2.8$	...	$0.67 \pm 0.06$	24.4	field
131249	18.40	$0.91 \pm 0.05$	226.0	0.2324	12.2	$2.12 \pm 0.06$	$0.2 \pm 0.9$	...	$0.68 \pm 0.05$	24.5	member
301131	18.44	$0.83 \pm 0.05$	668.3	0.2239	20.0	$2.35 \pm 0.1$	$0.0 \pm 0.7$	...	$0.65 \pm 0.06$	23.9	member
101100	18.46	$0.60 \pm 0.05$	125.5	0.2149	18.2	$1.76 \pm 0.03$	$6.3 \pm 0.8$	...	$0.67 \pm 0.02$	24.4	member
101523	18.48	$0.90 \pm 0.05$	135.0	0.2283	13.0	$2.31 \pm 0.07$	$-0.8 \pm 0.9$	...	$0.61 \pm 0.04$	23.0	member
500076	18.51	$0.58 \pm 0.05$	938.1	0.2178	13.1	$1.77 \pm 0.04$	$4.7 \pm 1.1$	...	...	...	near
500296	18.56	$-0.01 \pm 0.05$	1049.1	0.0658	...	...	...	...	...	...	field
101183	18.58	$0.87 \pm 0.05$	35.0	0.2303	12.1	$2.19 \pm 0.07$	$0.5 \pm 0.9$	...	$0.68 \pm 0.03$	24.4	member
200585	18.59	$0.81 \pm 0.05$	450.0	0.2236	14.0	$2.35 \pm 0.07$	$-0.6 \pm 0.8$	...	$0.58 \pm 0.04$	24.1	member
300063	18.60	$0.65 \pm 0.05$	570.2	0.2552	18.3	$1.75 \pm 0.03$	$7.3 \pm 0.7$	...	$0.50 \pm 0.06$	24.2	near
200500	18.61	$0.34 \pm 0.05$	303.5	0.1587	14.5	$1.55 \pm 0.03$	$6.2 \pm 1.0$	...	$0.57 \pm 0.04$	24.6	field
100818	18.63	$0.76 \pm 0.05$	201.0	0.2202	15.1	$2.15 \pm 0.05$	$1.8 \pm 0.8$	...	$0.67 \pm 0.06$	23.2	member
100908	18.64	$0.86 \pm 0.05$	32.8	0.2470	13.4	$2.2 \pm 0.06$	$1.3 \pm 0.8$	...	$0.62 \pm 0.04$	23.6	member
351002	18.67	$0.71 \pm 0.05$	766.5	0.2245	9.3	$1.89 \pm 0.07$	$7.7 \pm 1.6$	...	$0.44 \pm 0.04$	24.2	member
500354	18.73	$0.80 \pm 0.05$	886.5	0.2189	12.0	$2.2 \pm 0.1$	$1.6 \pm 1.2$	...	$0.64 \pm 0.05$	24.2	member
101573	18.75	$0.88 \pm 0.05$	109.3	0.2302	6.6	$2.87 \pm 0.21$	$-1.1 \pm 1.7$	...	$0.66 \pm 0.05$	23.8	member
101374	18.82	$0.86 \pm 0.05$	89.1	0.2192	12.3	$2.34 \pm 0.08$	$-0.0 \pm 0.9$	...	$0.71 \pm 0.05$	23.4	member
101190	18.83	$0.88 \pm 0.05$	50.2	0.2243	12.4	$2.57 \pm 0.09$	$-1.2 \pm 0.9$	...	$0.76 \pm 0.05$	24.5	member
300034	18.86	$0.52 \pm 0.05$	385.4	0.2262	24.8	$1.46 \pm 0.02$	$0.6 \pm 2.2$	$-4.5 \pm 1.3$	$0.73 \pm 0.05$	24.2	member
101992	18.87	$0.78 \pm 0.05$	205.6	0.1795	10.6	$2.16 \pm 0.09$	$1.3 \pm 1.2$	...	$0.84 \pm 0.07$	24.4	field
400724	18.90	$0.82 \pm 0.05$	1139.0	0.2810	10.0	$1.72 \pm 0.04$	$-0.2 \pm 1.0$	...	$0.56 \pm 0.03$	24.3	field
101033	18.90	$0.70 \pm 0.05$	78.3	0.2460	10.9	$1.75 \pm 0.05$	$-0.7 \pm 1.0$	$-52.4 \pm 4.0$	$0.55 \pm 0.08$	23.8	member
300814	18.90	$0.89 \pm 0.05$	386.5	0.2215	15.2	$2.07 \pm 0.05$	$-4.3 \pm 0.7$	...	$0.74 \pm 0.04$	24.2	member
201115	18.92	$0.82 \pm 0.05$	413.9	0.2362	12.1	$2.15 \pm 0.07$	$0.7 \pm 0.9$	...	$0.66 \pm 0.04$	24.6	member
301134	18.92	$0.84 \pm 0.05$	602.7	0.2287	15.7	$2.25 \pm 0.05$	$-1.9 \pm 0.7$	...	$0.74 \pm 0.06$	24.2	member
100930	18.96	$1.02 \pm 0.05$	186.7	0.2364	10.2	$2.31 \pm 0.09$	$-0.5 \pm 1.1$	...	...	...	member
300340	18.97	$1.15 \pm 0.05$	630.2	0.3168	8.6	$2.52 \pm 0.08$	$-3.5 \pm 1.0$	...	$0.61 \pm 0.05$	24.3	field
300753	18.99	$0.85 \pm 0.05$	615.4	0.2221	9.4	$2.42 \pm 0.11$	$4.4 \pm 1.5$	...	$0.61 \pm 0.07$	23.0	member
102210	19.00	$0.90 \pm 0.05$	233.5	0.2286	14.0	$2.6 \pm 0.14$	$0.0 \pm 1.3$	...	$0.75 \pm 0.05$	24.5	member
200792	19.02	$0.31 \pm 0.05$	505.2	0.2046	7.5	$1.66 \pm 0.08$	$12.4 \pm 2.0$	...	$0.49 \pm 0.06$	24.4	near
500538	19.03	$0.68 \pm 0.05$	821.3	0.2200	7.9	$1.72 \pm 0.07$	$4.3 \pm 1.5$	...	...	...	member
101930	19.04	$0.91 \pm 0.05$	150.4	0.2280	4.2	$2.77 \pm 0.36$	$1.4 \pm 2.9$	...	$0.81 \pm 0.03$	24.4	member
300413	19.04	$0.86 \pm 0.05$	330.1	0.1800	2.3	$1.38 \pm 0.17$	$10.2 \pm 5.5$	...	$0.48 \pm 0.05$	24.2	field
101462	19.04	$0.83 \pm 0.05$	170.2	0.2421	10.8	$2.31 \pm 0.08$	$0.2 \pm 1.0$	...	$0.61 \pm 0.06$	23.4	member
100956	19.06	$0.98 \pm 0.05$	24.0	0.2293	12.9	$2.29 \pm 0.07$	$0.8 \pm 0.9$	...	$0.68 \pm 0.09$	22.1	member
210569	19.07	$0.93 \pm 0.05$	293.5	0.2276	10.6	$2.13 \pm 0.08$	$3.8 \pm 1.3$	...	$0.60 \pm 0.06$	23.4	member

TABLE 1—*Continued*

PPP# (a)	$r$ (b)	$g-r$ (c)	$r_p$ (d)	$z$ (e)	S/N (f)	D4000 (g)	$H\delta$ (h)	[O II] (i)	$C$ (j)	$\mu_r$ (k)	Mem (l)
	19.07	$0.96 \pm 0.05$	85.8	0.2237	6.6	$1.82 \pm 0.11$	$3.4 \pm 2.3$	...	...	...	mem
500121	19.07	$0.83 \pm 0.05$	939.5	0.2302	10.1	$2.35 \pm 0.09$	$0.6 \pm 1.1$	...	...	...	mem
300425	19.07	$0.87 \pm 0.05$	737.4	0.2314	10.9	$2.04 \pm 0.06$	$3.1 \pm 1.3$	...	...	...	mem
101961	19.10	$0.94 \pm 0.05$	227.0	0.2220	9.3	$2.32 \pm 0.11$	$-0.2 \pm 1.3$	...	$0.69 \pm 0.06$	21.9	mem
100179	19.11	$0.88 \pm 0.07$	216.3	0.2252	7.0	$1.86 \pm 0.1$	$4.1 \pm 2.0$	...	$0.66 \pm 0.04$	24.5	mem
201208	19.11	$0.50 \pm 0.05$	591.6	0.2321	16.1	$1.41 \pm 0.02$	$1.6 \pm 0.7$	...	$0.58 \pm 0.03$	24.5	mem
200528	19.11	$0.53 \pm 0.05$	401.0	0.2318	13.1	$1.56 \pm 0.03$	$6.2 \pm 1.1$	$-5.6 \pm 2.6$	$0.51 \pm 0.03$	24.6	mem
300332	19.14	$1.00 \pm 0.05$	385.6	0.3067	5.9	$1.69 \pm 0.06$	$-2.2 \pm 1.5$	...	$0.47 \pm 0.04$	24.2	field
101077	19.14	$0.83 \pm 0.05$	9.8	0.2286	6.0	$1.97 \pm 0.13$	$3.2 \pm 2.5$	...	$0.56 \pm 0.05$	23.7	mem
100942	19.14	$0.90 \pm 0.05$	166.7	0.2328	7.7	$1.9 \pm 0.09$	$0.2 \pm 1.5$	...	$0.70 \pm 0.04$	24.5	mem
300442	19.15	$1.15 \pm 0.05$	552.5	0.3200	...	...	$-0.4 \pm 1.0$	...	$0.59 \pm 0.04$	24.1	field
200228	19.16	$1.01 \pm 0.05$	593.5	0.2323	5.2	$2.07 \pm 0.16$	$15.1 \pm 2.9$	...	$0.42 \pm 0.07$	22.2	mem
300450	19.18	$0.78 \pm 0.05$	536.2	0.2306	11.4	$2.09 \pm 0.07$	$3.6 \pm 1.2$	...	$0.61 \pm 0.04$	24.2	mem
102174	19.18	$0.73 \pm 0.05$	242.5	0.2215	10.2	$1.83 \pm 0.07$	$-0.8 \pm 1.1$	...	$0.79 \pm 0.05$	24.4	mem
101904	19.18	$0.86 \pm 0.05$	203.8	0.2353	9.9	$2.13 \pm 0.08$	$1.6 \pm 1.2$	...	$0.79 \pm 0.04$	24.3	mem
301347	19.20	$0.81 \pm 0.05$	586.0	0.2251	9.9	$2.05 \pm 0.08$	$3.2 \pm 1.4$	...	$0.51 \pm 0.04$	24.2	mem
100809	19.20	$0.85 \pm 0.05$	149.1	0.2293	10.1	$2.29 \pm 0.09$	$-1.4 \pm 1.1$	...	$0.72 \pm 0.03$	24.6	mem
301346	19.22	$0.93 \pm 0.05$	490.0	0.3179	9.3	$1.95 \pm 0.06$	$-0.7 \pm 0.9$	...	$0.57 \pm 0.07$	22.9	field
100995	19.23	$0.91 \pm 0.05$	48.5	0.2289	6.4	$2.41 \pm 0.18$	$-2.3 \pm 1.8$	...	$0.66 \pm 0.05$	24.5	mem
301249	19.25	$0.77 \pm 0.05$	658.6	0.2295	8.4	$1.94 \pm 0.08$	$5.8 \pm 1.7$	...	$0.57 \pm 0.03$	24.1	mem
201260	19.26	$0.84 \pm 0.05$	720.9	0.2221	9.0	$1.93 \pm 0.08$	$3.0 \pm 8.4$	...	$0.63 \pm 0.08$	22.2	mem
301306	19.27	$0.82 \pm 0.06$	600.7	0.2238	6.4	$2.15 \pm 0.13$	$5.5 \pm 2.2$	...	$0.62 \pm 0.04$	24.3	mem
101506	19.28	$0.69 \pm 0.07$	187.9	0.2818	9.0	$1.58 \pm 0.04$	$3.3 \pm 1.3$	...	...	...	field
301359	19.28	$0.62 \pm 0.06$	704.3	0.2245	13.5	$1.87 \pm 0.04$	$5.3 \pm 0.9$	...	$0.60 \pm 0.05$	24.1	mem
101106	19.29	$0.94 \pm 0.05$	23.7	0.2317	10.4	$2.14 \pm 0.08$	$2.9 \pm 1.3$	...	$0.63 \pm 0.07$	23.2	mem
501106	19.30	$0.64 \pm 0.06$	1177.8	0.2798	9.6	$1.85 \pm 0.05$	$4.4 \pm 1.4$	...	...	...	field
101861	19.31	$0.91 \pm 0.05$	164.8	0.1897	0.9	$-0.35 \pm 0.28$	...	...	$0.73 \pm 0.06$	24.5	field
500894	19.31	$0.58 \pm 0.06$	840.6	0.2246	9.5	$1.8 \pm 0.08$	$6.0 \pm 1.8$	...	$0.50 \pm 0.04$	24.3	mem
101136	19.32	$0.95 \pm 0.06$	24.7	0.2317	11.3	$2.49 \pm 0.09$	$-1.1 \pm 1.0$	...	$0.75 \pm 0.06$	23.9	mem
101850	19.33	$0.55 \pm 0.05$	186.7	0.2201	7.1	$2.18 \pm 0.13$	$2.5 \pm 2.0$	...	$0.50 \pm 0.04$	24.2	mem
100890	19.34	$1.04 \pm 0.05$	39.6	0.2283	5.7	$2.22 \pm 0.18$	$6.4 \pm 2.2$	...	$0.51 \pm 0.03$	24.4	mem
300185	19.36	$0.84 \pm 0.05$	725.0	0.2252	10.0	$2.46 \pm 0.11$	$-0.4 \pm 1.1$	...	$0.64 \pm 0.06$	23.3	mem
300816	19.36	$0.82 \pm 0.05$	505.9	0.2253	11.2	$2.06 \pm 0.07$	$-1.6 \pm 0.9$	...	$0.67 \pm 0.05$	24.3	mem
301046	19.38	$0.63 \pm 0.05$	710.3	0.2238	10.8	$1.65 \pm 0.05$	$4.4 \pm 1.3$	...	$0.56 \pm 0.05$	23.9	mem
101947	19.39	$0.94 \pm 0.05$	224.3	0.2284	7.7	$2.21 \pm 0.12$	$0.2 \pm 1.5$	...	$0.68 \pm 0.06$	22.1	mem
100165	19.39	$0.77 \pm 0.05$	238.7	0.2349	8.2	$2.01 \pm 0.09$	$1.9 \pm 1.4$	...	$0.57 \pm 0.04$	24.4	mem
101434	19.40	$0.96 \pm 0.05$	120.6	0.2299	9.7	$2.54 \pm 0.12$	$-0.7 \pm 1.2$	...	$0.79 \pm 0.05$	24.7	mem
350471	19.40	$0.28 \pm 0.05$	778.4	0.2559	17.1	$1.41 \pm 0.02$	$5.5 \pm 0.8$	$-19.3 \pm 1.5$	$0.56 \pm 0.04$	24.7	near
201049	19.42	$0.47 \pm 0.05$	747.0	0.2210	13.8	$-31.39 \pm 16.49$	$-0.9 \pm 1.1$	...	$0.58 \pm 0.04$	24.4	mem
200514	19.43	$0.64 \pm 0.05$	562.9	0.3216	...	...	$4.4 \pm 0.9$	$-5.9 \pm 1.4$	$0.65 \pm 0.07$	21.9	field
301011	19.44	$0.21 \pm 0.06$	319.2	0.1029	...	...	$16.4 \pm 4.2$	...	$0.45 \pm 0.03$	24.3	field
101054	19.44	$0.86 \pm 0.06$	98.1	0.2234	9.5	$1.96 \pm 0.08$	$0.9 \pm 1.2$	...	$0.69 \pm 0.06$	24.4	mem
300671	19.44	$0.84 \pm 0.05$	627.5	0.2226	8.2	$2.17 \pm 0.1$	$-0.6 \pm 1.4$	...	$0.56 \pm 0.07$	24.2	mem
201045	19.45	$0.64 \pm 0.06$	454.1	0.2264	11.5	$1.69 \pm 0.05$	$3.4 \pm 1.2$	...	$0.66 \pm 0.08$	22.1	mem
100039	19.45	$0.83 \pm 0.05$	217.1	0.2274	15.0	$2.1 \pm 0.06$	$0.0 \pm 0.9$	...	$0.86 \pm 0.06$	24.5	mem
100693	19.46	$0.90 \pm 0.05$	70.0	0.2291	6.0	$2.32 \pm 0.18$	$-0.6 \pm 1.8$	...	$0.75 \pm 0.05$	24.5	mem
100773	19.46	$0.84 \pm 0.05$	77.2	0.2313	10.0	$2.18 \pm 0.09$	$3.4 \pm 1.2$	...	$0.69 \pm 0.05$	24.4	mem
301078	19.47	$0.80 \pm 0.05$	559.0	0.2294	9.4	$2.42 \pm 0.11$	$1.0 \pm 1.2$	...	$0.64 \pm 0.05$	24.2	mem
200648	19.49	$0.58 \pm 0.05$	486.7	0.3076	8.3	$1.56 \pm 0.04$	$1.5 \pm 1.1$	$-8.4 \pm 2.6$	$0.67 \pm 0.05$	24.6	field
300475	19.50	$0.67 \pm 0.06$	523.9	0.2248	12.2	$1.54 \pm 0.04$	$-0.6 \pm 0.9$	...	$0.64 \pm 0.05$	24.1	mem
301195	19.51	$0.33 \pm 0.06$	480.6	0.2221	7.7	$1.42 \pm 0.05$	$3.9 \pm 1.9$	...	$0.49 \pm 0.03$	24.3	mem
301348	19.52	$0.37 \pm 0.06$	544.3	0.1744	14.0	$1.62 \pm 0.04$	$6.8 \pm 1.4$	...	$0.60 \pm 0.05$	24.2	field
101800	19.52	$0.89 \pm 0.06$	197.4	0.2340	4.1	$2.15 \pm 0.21$	$6.7 \pm 3.4$	...	$0.64 \pm 0.05$	24.4	mem
101269	19.53	$0.86 \pm 0.05$	78.1	0.2432	9.1	$2.31 \pm 0.1$	$0.9 \pm 1.2$	...	$0.67 \pm 0.05$	24.4	mem
100816	19.54	$0.86 \pm 0.05$	224.1	0.2312	6.4	$2.82 \pm 0.22$	$-1.7 \pm 1.9$	...	$0.75 \pm 0.05$	23.8	mem
201286	19.55	$0.88 \pm 0.05$	456.1	0.2287	8.7	$1.98 \pm 0.08$	$0.8 \pm 1.4$	...	$0.63 \pm 0.04$	24.8	mem

TABLE 2  
 WAVELENGTHS OF THE LINE AND CONTINUUM REGIONS

	Line	Continuum 1	Continuum 2
D4000	...	3750 – 3950 Å	4050 – 4250 Å
O II 3727	3713 – 3741 Å	3653 – 3713 Å	3741 – 3801 Å
H $\delta_{nar}$	4082 – 4122 Å	4030 – 4082 Å	4122 – 4170 Å
H $\delta_{wid}$	4088 – 4116 Å	4030 – 4082 Å	4122 – 4170 Å

TABLE 3  
 ABELL 2390 AND SIMILAR BUTCHER-OEMLER CLUSTERS

Cluster	$z$	$C_{BO}$	$R_{30}$ (arcmin)	$f_b$
Abell 2390	0.231	0.49	3.0	$0.14 \pm 0.05$
Abell 1961	0.232	0.50	3.4	$0.10 \pm 0.05$
Abell 1942	0.224	0.56	2.8	$0.17 \pm 0.05$

# GALAXY EVOLUTION IN ABELL 2390

R. G. Abraham<sup>1</sup>

Institute of Astronomy, University of Cambridge  
Madingley Road, Cambridge CB3 0HA UK<sup>2</sup>

and

Dominion Astrophysical Observatory, Herzberg Institute of Astrophysics  
National Research Council of Canada  
5071 W. Saanich Rd., Victoria B.C. V8X 4M6 Canada  
abraham@ast.cam.ac.uk

Tammy A. Smecker-Hane<sup>1,3</sup>, J. B. Hutchings

Dominion Astrophysical Observatory, Herzberg Institute of Astrophysics  
National Research Council of Canada  
5071 W. Saanich Rd., Victoria B.C. V8X 4M6 Canada  
smecker@carina.ps.uci.edu, hutchngs@dao.nrc.ca

R. G. Carlberg<sup>1</sup>, H. K. C. Yee<sup>1</sup>

Department of Astronomy, University of Toronto,  
Toronto, Ontario, M5S 1A7 Canada  
carlberg@moonray.astro.utoronto.ca, hyee@makalu.astro.utoronto.ca

Erica Ellingson<sup>1</sup>

CASA, University of Colorado  
Boulder, Colorado 80309-0389  
e.elling@pisco.colorado.edu

Simon Morris<sup>1</sup>, J. B. Oke, Michael Rigler<sup>1</sup>

Dominion Astrophysical Observatory, Herzberg Institute of Astrophysics  
National Research Council of Canada  
5071 W. Saanich Rd., Victoria B.C. V8X 4M6 Canada  
simon@dao.nrc.ca, oke@dao.nrc.ca, mrigler@microsoft.com

## ABSTRACT

---

<sup>1</sup>Guest Observer, Canada France Hawaii Telescope, which is operated by the NRC of Canada, CNRS of France, and the University of Hawaii.

<sup>2</sup>Current address.

<sup>3</sup>Current address: Department of Physics, University of California, Irvine, CA 92717.

The galaxy population in the intermediate-redshift ( $z = 0.228$ ) rich cluster Abell 2390 is investigated. We present velocities, colors, and morphological information for an exceptionally large sample of 323 galaxies (216 cluster members) in a  $46' \times 7'$  ( $6 h^{-1} \text{ Mpc} \times 1 h^{-1} \text{ Mpc}$ ) strip centered on the cD galaxy. This sample of confirmed cluster members is second only to that for the Coma cluster in terms of sample size and spatial coverage in the cluster rest frame, and is the first to trace the transition between a rich cluster and the field at intermediate redshift. The galaxy population in the cluster changes gradually from a very evolved, early-type population in the inner  $0.4 h^{-1} \text{ Mpc}$  of the cluster to a progressively later-type population in the extensive outer envelope of the cluster from 1 to  $3 h^{-1} \text{ Mpc}$  in radius. Radial gradients in galaxy  $g - r$  color, 4000 Å break, H $\delta$  and [O II] line strengths and morphology are seen in the cluster, and are investigated by comparing the data to models computed with the GISSEL spectral synthesis package. The results suggest that the cluster has been gradually built up by the infall of field galaxies over  $\sim 8 \text{ Gyr}$  and that star formation has been truncated in infalling galaxies during the accretion process. The morphological composition of the cluster is shown to be consistent with such a scenario. If true for other clusters, infall-truncated star formation as seen in Abell 2390 may explain both the Butcher-Oemler effect and the large fraction of S0 galaxies in clusters. Only  $\lesssim 5\%$  of the galaxies observed in Abell 2390 exhibit evidence for star formation at levels stronger than those seen in typical late-type systems. This suggests that starbursts do not play a major role in driving cluster galaxy evolution at the redshift of Abell 2390, although infall-induced starbursts leading to truncated star-formation may have played a role in the earlier history of the cluster. Evidence is found for at least one subcomponent on the West side of the cluster, which is likely to be infalling at the epoch of observation.

## 1. INTRODUCTION

Within the hierarchical gravitational instability theory, clusters of galaxies are created by merging of smaller clusters. Such merged clusters may have no memory of their initial conditions, or they may retain the radial gradients of the progenitors. More specifically, “violent relaxation” (Lynden-Bell 1967) erases nearly all memory of the initial structures (but see Quinn, Salmon, & Zurek 1986), whereas steady accretion formation (Gunn & Gott 1972) builds the cluster slowly and continuously over a Hubble time, so that the orbits remain stratified in a radial age sequence. Nearly equal mass mergers will be quite “violent”, but the steady accretion of individual galaxies and small groups on to a pre-existing cluster leaves the structure of the initial cluster relatively unaffected. The ability of the cluster to continue to accrete material at low redshift depends on the initial overdensity profile of the cluster and  $\Omega$  (Gunn & Gott 1972).

If a cluster is uniformly mixed then we presume that the last merger was quite violent. Cluster galaxies are generally red, and the combination of their mean color and the *dispersion* in color allows a limit to be put on how closely in time the galaxies formed, and thus on the epoch of initial galaxy formation. Observed gradients in galaxy populations can be used to trace the cluster’s accretion history, and to test simple galaxy evolution models. There is likely to be a close relationship between population gradients in clusters and the “Butcher-Oemler Effect” (the increase in the fraction of blue cluster members with redshift). HST observations of the intermediate redshift clusters CL 0939+4713 ( $z = 0.41$ ; Dressler et al. 1994), Abell 370 ( $z = 0.39$ ; Couch et al. 1994), and AC 114 ( $z = 0.31$ ; Couch et al. 1994) have shown that in these three clusters the relative fraction of spirals, S0 galaxies, and ellipticals is similar to that seen in the *field* at the current epoch. These observations suggest that the Butcher-Oemler effect is mostly due to an excess population of late-type systems, and not due to a population of starbursting, early-type systems. If CL 0939+4713, Abell 370, and AC 114 (the only clusters for which morphological studies at  $z \sim 0.3 - 0.4$  have been published) are representative of rich clusters at intermediate redshift, then the cluster galaxy population has evolved since  $z \sim 0.4$  into the early-type-dominated population seen in nearby clusters (Dressler 1980). The narrow color-magnitude envelope for the red galaxies in the clusters studied with HST led both Dressler et al. (1994) and Couch et al. (1994) to conclude that the old population in these clusters is similar to ellipticals and S0s seen at the current epoch, and hence that galaxy evolution in clusters is dominated by the fading or destruction of cluster spirals.

Other evidence for cluster galaxy evolution was discovered by Dressler & Gunn (1983), who found that a substantial number of galaxies in intermediate redshift clusters have enhanced Balmer absorption for their color. These authors coined the term “E+A galaxy”

to describe these objects, noting that their spectra could be matched with a mixture of an elliptical galaxy and an A-type stellar population, and that their colors were intermediate between those of early-type systems and spirals. Since Balmer lines are enhanced as the main-sequence turnoff moves through A stars, which occurs  $\sim 1$  Gyr after star-formation (or a starburst) ceases, the spectroscopic characteristics and colors of E+A galaxies have led most authors to conclude that E+A systems are the remnants of starbursts that have recently occurred in old galaxies. However, others (*e.g.* Couch & Sharples 1987) show that it is hard to distinguish between 1 Gyr old starbursts in early-type systems and late-type systems whose star-formation has simply been truncated without an initial starburst, and in view of this ambiguity prefer the term “H $\delta$ -strong” (HDS) to “E+A”. More recently, Charlot & Silk (1994) have shown that, solely on the basis of optical colors and spectra, it is virtually impossible to distinguish between a major starburst in an elliptical and one in a spiral if star formation ceases after the burst. The only unambiguous way to identify these starbursts is to catch them *during* the burst when their [O II] emission is strong and their colors are blue.

In this paper we examine the galaxy population in the intermediate redshift cluster Abell 2390 ( $\alpha_{1950} = 21 : 51 : 14.3$ ,  $\delta_{1950} = +17 : 27 : 34.9$ ,  $z = 0.228$ ). The data were obtained as part of the Canadian Network for Observational Cosmology (CNOC) dynamical survey of X-ray-luminous clusters of galaxies (Carlberg et al. 1994). Abell 2390 is a large, rich cluster with a sizable hot intracluster medium ( $L_x = 5.5 \times 10^{44}$  erg s $^{-1}$ ; McMillan, Kowalski, & Ulmer 1989). We use the observed colors, spectral features and morphologies of the galaxies to put limits on the star-formation histories of cluster galaxies and on the cluster’s accretion history. The plan of this paper is as follows. In §2, we describe our spectroscopic and photometric data and analysis, and outline the automated procedure used to obtain the morphological classifications. In §3, we discuss the rich spatial and velocity structure of the cluster. We demonstrate that Abell 2390 contains a very old, red, centrally condensed component, and that galaxies in the extensive outer envelope of the cluster show a radial gradient in which bluer, later type galaxies are found systematically at larger radii. We also identify a distinct group of galaxies (red as well as blue: the ‘NW Group’) that appear to constitute a small cluster that is merging with Abell 2390. In §4, we discuss the galaxies with current star formation ([O II] emission line galaxies) and those galaxies which have recently experienced a significant decrease in their star formation rates (strong Balmer absorbers). In §5, we discuss how we have used the GISSEL spectral synthesis package (Bruzual & Charlot 1993) to calculate the line strengths and colors of galaxies for various galaxy evolution models. In §6, we compare the data with these models. In §7, we show that the gradients in galaxy color, spectroscopic line measures, and morphology are consistent with a scenario in which the the outer part of the cluster is built



up slowly over a Hubble time, while star formation is truncated in infalling galaxies. In this picture, the radial gradients in Abell 2390 are due to systematic changes in the ages of the stellar populations in the galaxies as a function of radius. Abell 2390 is similar to other rich clusters at intermediate redshifts, and we speculate that truncated star formation may play an important role in the Butcher-Oemler effect and lead to the formation of cluster S0 galaxies. We also discuss evidence for merging and interactions in our imaging data. Our conclusions are summarized in §8.

## 2. OBSERVATIONS AND DATA REDUCTION

### 2.1. Optical spectroscopy and imaging

Abell 2390 was observed in June and October 1993 using the MOS arm of the MOS/SIS multi-object spectrograph (Le Fevre et al. 1993), mounted at the f/8 focus of the 3.6 meter Canada-France-Hawaii Telescope (CFHT). The observing strategy and spectroscopic reduction process are described in detail in Yee, Ellingson, & Carlberg (1996). Images in Cousins R and Gunn  $g$  filters were also obtained through the spectrograph in order to design the aperture masks; these are described in Section 2.3 below. Photometry was calibrated to the Gunn  $g$  and  $r$  system. The extracted spectra cover the wavelength range 4300 – 5600 Å (3500 – 4550 Å in the rest frame of the cluster) with a dispersion of 3.45 Å/pixel and a resolution of 15.5 Å. The spatial scale at the rest frame of the cluster is  $430''/(h^{-1} \text{ Mpc})$ . A total of 323 redshifts covering a  $46' \times 7'$  strip (five slightly overlapping MOS fields centered on the cD galaxy) were obtained. Of these, 233 galaxies have redshifts in the range  $0.20 \leq z \leq 0.265$ , and 216 of these are considered to be cluster members (our criteria for determining cluster membership are described in §3.1). A complete catalog of cluster and field galaxies in our sample is given in Yee et al. (1996). Table 1 lists photometry, velocities, identification numbers (from Yee et al. 1996), and new spectroscopic and morphology measurements for the galaxies discussed in the present paper.

As with all surveys, selection effects play an important role in defining the present sample. In order to minimize selection anti-bias against close pairs, spectra for the crowded inner fields were obtained with 2 or 3 aperture masks. Even so, selection biases of order 30% remain over the surface of the cluster, but these can be accurately calibrated from our known selection function. A detailed completeness plot for the current dataset is given in Yee et al. (1996). As a rough guide, the cumulative completeness of the spectroscopic sample is over 80% to  $r = 20.0$  mag and  $\sim 60\%$  to  $r = 21.0$  mag. (The corresponding differential completeness rates at these magnitude limits are 74% and 30%, respectively). In Yee et al. (1996) it is shown that the present sample is unbiased with respect to color

for  $r < 21$  mag. Beyond  $r = 21$  mag completeness drops rapidly and is a strong function of the color, because redshifts are more easily derived from blue galaxies with [O II] emission lines. Hence in this paper the sample will be restricted to galaxies with  $r \leq 21.0$ . Since  $r = 21$  mag corresponds to  $M_V \sim -19$  mag at  $z = 0.23$  (assuming  $H_o = 75 \text{ km s}^{-1} \text{ Mpc}^{-1}$ ), the spectroscopic dataset probes  $\sim 1.5 - 2$  mag fainter than  $M^*$  in the cluster luminosity function (assuming  $M_{BT}^* = -20.3$  mag, as found by Efstathiou, Ellis, & Peterson 1988).

The completeness limits for object detection on our images varies from field to field, as a result of differing integration times on our CCD frames (900s in the central field, 600s in the outer fields). The detection completeness limit spans a range from 23.5 to 24 mag for  $r$ , and 23.2 to 24 mag for  $g$ . A variable PSF across the MOS field limits successful star-galaxy separation to objects with  $r \leq 23.5$  mag. (The quality of the images was limited by the MOS optics rather than by observing conditions; the FWHM of the PSF varied between  $0.9'' - 1.3''$ ). Taken together, the imaging data are complete to  $M_U \approx -17.0$  mag and  $M_V \approx -16.6$  mag in the rest frame of the cluster.

## 2.2. Spectroscopic Measures

The two-dimensional spectral images were cleaned of cosmic rays and extracted (with variance-weighting) using the IRAF “apextract” package. Spectra were wavelength-corrected, flux-calibrated and extinction-corrected to bring all spectra to the same system. Redshifts and the confidence parameter  $R_{xcor}$  were derived using cross-correlation techniques. Details of the data reduction procedure are given in Yee, Ellingson, & Carlberg (1996), and the final photometric/spectroscopic catalog, together with completeness and selection functions, is presented in Yee et al. (1996). In this paper additional measurements will be presented for all spectra in Yee et al. (1996) with derived redshifts. These measurements include the  $4000\text{\AA}$  break (D4000, *cf.* Hamilton 1985), and the equivalent widths of [O II]  $3727\text{\AA}$  and  $H\delta$ . In the present paper the signal-to-noise ratio (S/N) of the spectra are quantified in terms of the mean S/N in the rest frame  $4050 - 4250 \text{\AA}$  region.

Equivalent widths at the observed redshift of each spectrum were calculated assuming fixed rest wavelengths for each line and pair of continuum regions. The observed equivalent widths were then converted to the rest frame by dividing by  $(1 + z)$ . The definitions of the line and continuum regions used in the present work are shown in Table 2. The definitions are based on those of Dressler & Shectman (1987) but were modified to be compatible with the spectral resolution of both the observed data and the model spectra generated by the GISSEL spectral synthesis package (Bruzual & Charlot 1993). The equivalent widths for the observed and model spectra in this paper were computed in identical ways. The noise in

the spectrum of the sky background was used in calculating the measurement error for each spectral feature following the formulae in Bohlin et al. (1983) Appendix A. Internal checks based on multiple observations of the same galaxies through different spectroscopic masks verify that the errors calculated in this way are a good description of the uncertainties in our spectroscopic measurements.

One of the most important line measures is  $H\delta$ , because it is used to identify galaxies which have recently ceased vigorous star formation. The actual width of the line varies as the stellar population evolves and metallic absorption lines begin to appear in the nearby continuum. Extreme care has been taken in measuring  $H\delta$  in both the observed spectra and the models, and our methods have been tested against high resolution extant spectra of stars and galaxies. The continuum at  $H\delta$  was fitted using relatively wide bandpasses and then re-fitted rejecting the points lower/higher than  $-5/+13$  times the average deviation from the initial fit. This simple iterative procedure nicely masks out absorption features and noise spikes and leads to a more robust definition of the true continuum. In addition, equivalent widths for two line bandpasses that are  $28 \text{ \AA}$  and  $40 \text{ \AA}$  wide and centered on  $H\delta$  were calculated ( $H\delta_{\text{nar}}$  and  $H\delta_{\text{wide}}$ , respectively). For the  $H\delta$  measurement, the narrower bandpass is adequate for absorption  $< 2 \text{ \AA}$ , but when the absorption is stronger and the wings of the line broader then the equivalent width calculated with the wider bandpass needs to be used in order to adequately span the full range of  $H\delta$  absorption strengths. Thus the definition for  $H\delta$  equivalent width used in this paper is:  $H\delta = H\delta_{\text{nar}}$  if  $H\delta_{\text{nar}} < 2 \text{ \AA}$ , and  $H\delta = H\delta_{\text{wide}}$  if  $H\delta_{\text{nar}} > 2 \text{ \AA}$ .

### 2.3. Morphological parameters

The morphologies of the galaxies in Abell 2390 were determined using the automated system of Abraham et al. (1994), which is quite similar to the method proposed by Doi, Fukugita, & Okamura (1993). The fundamental parameter of this system is a galaxy’s central concentration of light,  $C$ . This parameter is determined from the intensity-weighted moments of the galaxy images. It is emphasized that  $C$  values are morphological *measurements*, rather than classifications. Because it is based on the central concentration of light, the Abraham et al. (1994) system bears more similarity to Morgan’s Yerkes system (Morgan 1958) than it does to the standard Hubble system. However, it has long been known (Shapley 1927) that central concentration measurements can be used to distinguish effectively between early and late galaxy types. Determining more subtle distinctions between galaxies on the Hubble sequence (eg. distinguishing ellipticals from S0 galaxies) cannot be done from  $C$ , but in any case such distinctions cannot be made visually at the

redshift of Abell 2390 from our images. The main advantages of the automated classification system are (a) objectivity, (b) applicability at redshifts where classifications based on the Hubble system are difficult to make, and (c) the existence of well-defined uncertainties on the morphological measurements. As described in Abraham et al. (1994), the values of  $C$  determined for each galaxy result from a two-step reduction process. Direct measurements of  $C$  were first made using code added to the FOCAS galaxy detection package (Valdes 1982). In the second stage of the reduction process these  $C$  measurements were corrected for the effects of seeing degradation, using the results from Monte Carlo simulations.

For un-blended and fairly smooth galaxies, the central concentration of light was determined within an area enclosed by an isophotal surface brightness limit that is  $2.5\sigma$  above the noise in the sky background. Since our images span a range of exposure times between 600s and 900s, the surface brightness of the limiting isophotes for the unblended galaxy population range between  $\mu_r = 24.1 - 24.5 \text{ mag/arcsec}^2$ . Simulations indicate that a change of  $\sim 0.4 \text{ mag/arcsec}^2$  in the isophotal limit can change the measured  $C$  values by  $\sim 0.03$ , which is small compared to the measurement errors inherent in determining  $C$ . For blended or highly distorted galaxies, the limiting isophote determined by FOCAS is substantially higher than the  $2.5\sigma$  sky noise limit. (FOCAS continuously raises the limiting isophotal level when a detected object’s isophote encloses several maxima, until only a single maximum is enclosed.) Since galaxies with high limiting isophotes correspond to blended or distorted objects, high isophotal limits flag possible merger candidates. Approximately 20% of the cluster members had high limiting isophotes ( $\mu_r < 23.5 \text{ mag/arcsec}^2$ ). However, the majority of these objects correspond to smooth-looking galaxies with stars or faint galaxies superposed on the galaxy images, rather than to obviously distorted interacting or merging systems. As discussed in Section 7 below, higher resolution images are required in order to determine unambiguously the rate of mergers and interactions in Abell 2390.

### 3. SPATIAL-VELOCITY STRUCTURE AND SUBCLUSTERING

The spatial distribution of the spectroscopic sample is shown in Figure 1. The central core of the cluster spans approximately  $400''$  ( $0.93 h^{-1} \text{ Mpc}$ ) on either side of the cD galaxy (which is assumed to mark the spatial origin of the cluster throughout this paper), before breaking up into structures whose proximity in velocity space (discussed below) suggests that they are gravitationally bound to the cluster. These structures are illustrated more clearly in Figure 2, which shows the spatial map of the cluster sliced into redshift “channels”.

For this paper, cluster membership is defined in a simple (statistical) way using

## Distributions of Galaxies in Abell 2390 Fields

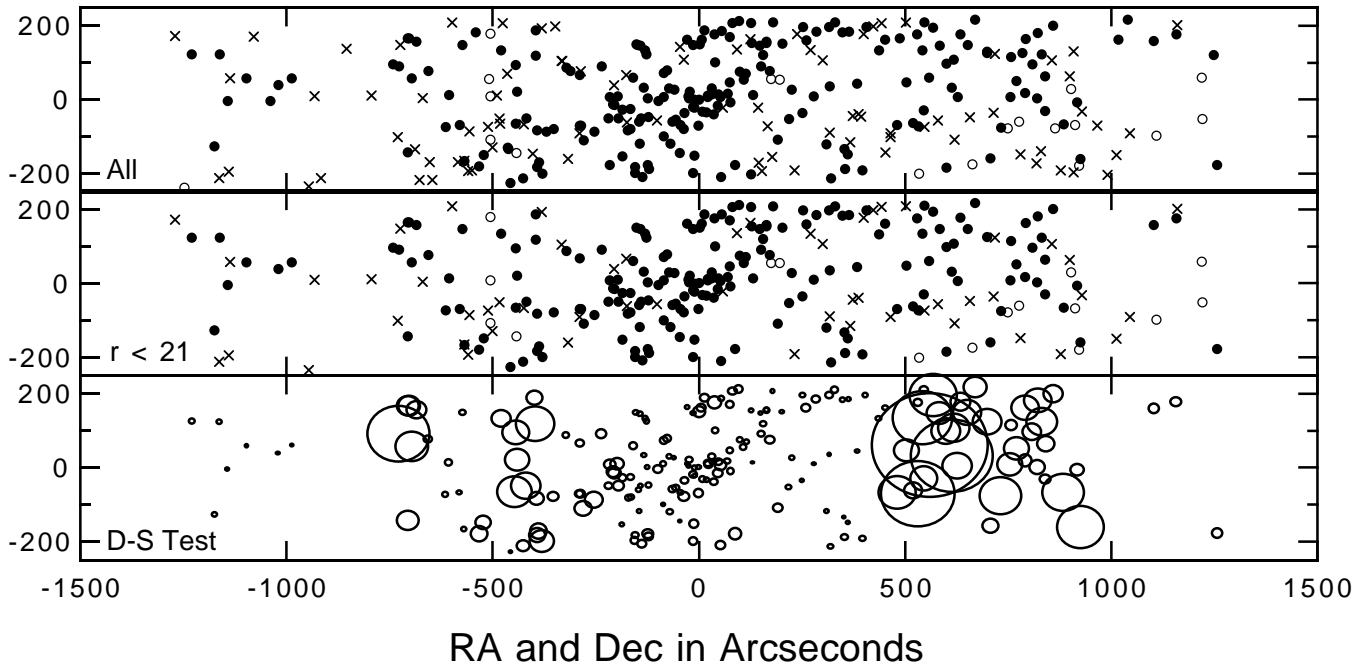


Fig. 1.— The spatial distribution of galaxies in the Abell 2390 sample. Solid circles denote cluster members, open circles denote “near field” galaxies (see text), and crosses denote field objects. (Top) All galaxies with known redshifts. (b) Galaxies brighter than  $r = 21$  mag (the restricted sample analyzed in the present work). (c) The results from a Dressler-Shectman test for spatial-velocity substructure. The radii of the circles are proportional to  $e^{\delta}$ , where  $\delta$  is the Dressler-Shectman subclustering estimator (Dressler & Shectman 1988).

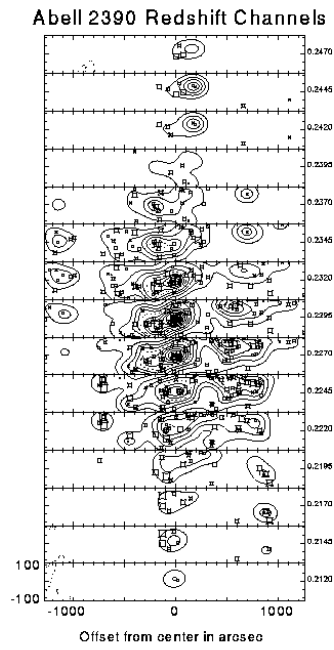


Fig. 2.— Redshift channels showing the distribution of cluster members in both spatial and velocity dimensions. The rich structure of our dataset in spatial-velocity space is obvious. The distribution of points in each panel has been smoothed with an angular Gaussian of FWHM  $80''$  in the spatial dimensions and 0.0025 in the redshift dimension. The area of each plot symbol is proportional to the luminosity of the galaxy.

the redshift–projected radius distribution of red galaxies shown in Figure 3 (the precise definition for “red” and “blue” galaxies adopted in the present work is given in the next section). Red galaxies appear well-separated from the field and are assumed to trace the boundaries of the cluster. The two straight lines in Figure 3 are used to define the border between cluster and field. This definition is purely empirical, but the clear absence of red galaxies outside the boundaries suggests that a cut made solely on the basis of redshift would include a further  $\sim 15$  high velocity blue galaxies that are unlikely to know about the cluster structure, even for high  $\Omega$  (Regős & Geller 1989). These blue objects may be infalling, and hence the field galaxy population is subdivided into “far field” objects that are outside the  $0.2 \leq z \leq 0.265$  redshift range, and “near field” objects that are inside the redshift range but outside the boundaries shown in Figure 3. The adopted definition for cluster members may still include a few infalling galaxies in the cluster, but the main goal of this paper is to highlight the transition in galaxy properties from the cluster center to the outer cluster while minimizing contamination from the field at large radii. The degree of contamination by field galaxies due to the “finger of god” effect (the elongation in redshift space of clusters due to their high velocity dispersion) can be estimated as follows (Koo 1988). The loci in Figure 3 trace out a total volume of  $\sim 500h^{-3} \text{ Mpc}^3$  over the rectangular configuration of our dataset, which is considerably larger than the physical volume occupied by the cluster. The degree of contamination by field galaxies is dependent mostly upon the richness and geometrical configuration of the large scale structure in which the cluster is embedded. If one assumes a galaxy density of  $< 1 \text{ galaxy}/100 \text{ Mpc}^3$  (typical of the field) then the expected contamination is only a few galaxies, which is negligible given our large sample. Of course it is possible that the cluster is embedded in a particularly rich component of large scale structure (which would result in greater contamination), but this seems unlikely from the redshift “pie” diagram given in Carlberg et al. (1995). It is emphasized that the conclusions in this paper are not strongly sensitive to the precise shape of the boundaries in Figure 3. Our  $r < 21\text{mag}$  sample is therefore composed of 199 cluster members, 14 near field galaxies, and 56 field galaxies.

The previous figures suggest that the cluster is composed of two or three main clumps, embedded in a sparsely-distributed envelope of galaxies. This visual impression is supported by the results from a Dressler-Shectman test (the bottom panel in Figure 1), which indicates that global substructure is significant with over 99.9% confidence. The strongest correlated motions occur over an extended region on the West side of the cluster. The Dressler-Shectman test is not sensitive to structure that is resolved in velocity space but is spatially superposed, so the test is not ideal for investigating velocity correlations amongst galaxies in the inner part of Abell 2390. For example, there is a remarkably low velocity spread among the innermost group of red galaxies (see Figure 3) in the cluster, suggesting

that the inner part of the central component of the cluster is dynamically “cold”. This is not evident in the results from the Dressler-Shectman test.

While the general presence of substructure in Abell 2390 seems clear, the identification of small physical subclumps from cluster catalogs is difficult to undertake reliably (West & Bothun 1990), and in this paper we will concentrate only on the two most obvious components seen in Figures 1 and 2. The first of these is the main cluster component centered on the cD. This dominates the central 400'' of the cluster, and in the next section it is shown that the red colors, evolved spectra, and early-type morphologies in this component are very uniform. The second obvious component in our spatial-velocity diagram is the “NW Group”, the (lower redshift) concentration to the northwest of the main central component of the cluster, at projected radius  $\simeq 650''$ . There are some 20 galaxies in this group, whose mean color is also significantly redder than that of their surroundings, and whose co-added spectrum shows them to be similar to the evolved galaxies at the cluster center. It appears likely that this is the core of a smaller cluster that is being accreted on to the main component of Abell 2390. Indeed, a simple two-body analysis suggests that this group is at least weakly bound to the cluster. In Figure 4 we show the result of a two-body calculation based upon the simple criterion derived by Beers, Geller, & Huchra (1982) for gravitational binding in subclumps:

$$V_{rel}^2 R_p < 2GM_{tot} \sin^2 \alpha \cos \alpha, \quad (1)$$

where  $M_{tot}$  is the total cluster mass,  $V_{rel}$  is the relative velocity between the two components along the line of sight,  $R_p$  is their projected separation, and  $\alpha$  is the angle between the plane of the sky and the line joining the centers of the two components. The NW Group is bound for most choices of  $H_o$  and  $\alpha$ .

## 4. THE GALAXY POPULATION

### 4.1. Blue Galaxies

The color-magnitude relationship in Abell 2390 is shown in Figure 5. Iteratively fitting the E/S0 sequence as a straight line using a chi-squared minimization and excluding cluster galaxies  $\pm 0.15$  mag outside the fit gives the following color-magnitude relationship:

$$(g - r) = 1.32(\pm 0.14) - 0.024(\pm 0.007) \times r.$$

The scatter in this relationship is largely due to a strong radial color *gradient* in the color of the old galaxy locus in the cluster (Figure 6). Normalizing colors to  $r = 19$  using



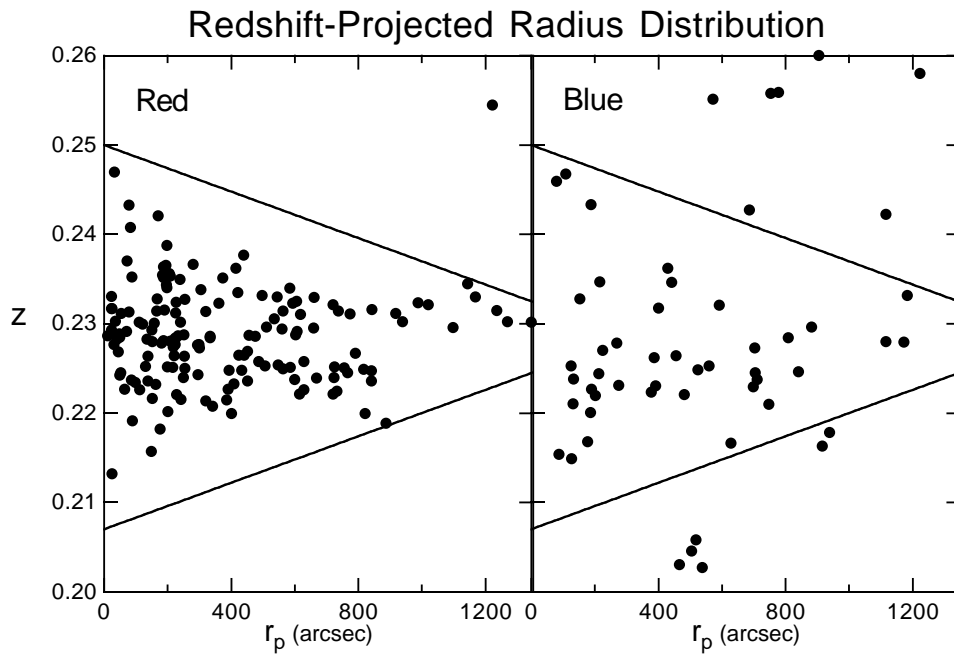


Fig. 3.— The redshift-projected radius distribution for red (left) and blue (right) galaxies. The well-defined distribution of red cluster members provides the basis for our definition of cluster and field membership (solid lines). See text for our definition of red and blue objects.

## Gravitational Binding of the NW-Group

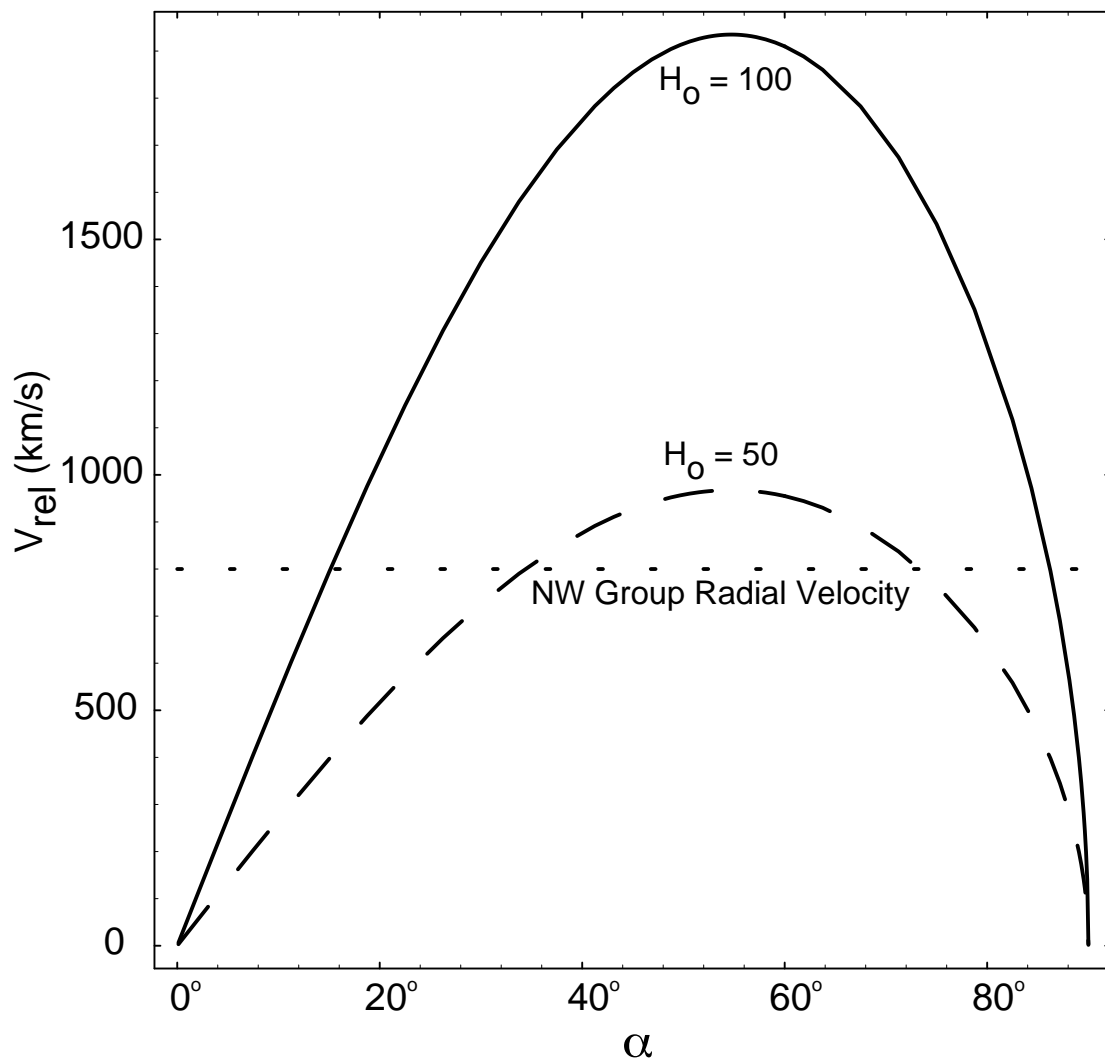


Fig. 4.— The bound and unbound regions in the  $(V_{rel}, \alpha)$  plane for the “NW-Group” in Abell 2390.  $\alpha$  is the angle between the plane of the sky and the line joining the centers of the two components. All points below the curves are gravitationally bound. The calculations assume a mass for the cluster of  $1.1 \times 10^{15} M_\odot$ , the lower limit to virial mass of the cluster determined by Carlberg et al. (1995). If the Hubble constant is high or if dark matter does not trace the luminous matter in Abell 2390 (as claimed by Carlberg et al. 1995) the NW-Group is likely to be bound.

the above color-magnitude relationship and computing the best fit line for the E/S0 ridge in the color-radius plane, we obtain the following relationship for the normalized color of the red galaxy population as a function of projected radius  $r_p$ :

$$(g - r)_{r=19} = 1.05 - 0.079 \log r_p$$

The color-radius relationship for the red galaxies is only approximately linear in  $\log r_p$ . The slope of the relationship appears shallower for the inner cluster and steeper for  $r_p \gtrsim 200'' = 0.46 h^{-1} \text{ Mpc}$ . The spread in red galaxy colors is approximately 0.15 mag over the full range of radius.

The radial gradient in the colors of the red galaxies leads to the following definition for the blue population. *Blue objects are defined to be those galaxies at least 0.25 mag bluer in  $g - r$  than the color of the red galaxy locus at the projected radius of each individual galaxy.* The cutoff at  $\Delta(g - r) = 0.25$  was chosen because this corresponds closely<sup>4</sup> to the rest-frame  $B - V = 0.20$  offset adopted by Butcher & Oemler (1984).

The spatial distributions of red and blue objects are shown in panel (a) of Figure 7. The distribution of colors in the galaxy population is qualitatively similar to that seen in local relaxed clusters, with a strong concentration of red galaxies in the cluster center and an increasing fraction of blue galaxies as a function of radius. The NW Group is also dominated by red galaxies, the reddest colors of which appear to be slightly ( $\sim 0.1$  mag) bluer than the reddest galaxies at the center of the main body of the cluster.

## 4.2. Line Emitting Galaxies

The distribution of [O II] emitters ( $2\sigma$  detections confirmed by visual inspection) is shown in panel (d) of Figure 7. Fourteen cluster members, six near field galaxies, and fourteen field galaxies exhibit [O II] emission. Assuming Poisson statistics, the fraction of detected line-emitters is therefore estimated at only  $7 \pm 1\%$  amongst cluster members,  $43 \pm 16\%$  in the near field population, and  $25 \pm 7\%$  in the field. We note that the emission line field sample may be biased with redshift due to the presence of a band-limiting filter and because of the low quantum efficiency of the CCD at blue wavelengths. However, our detection of [O II] in cluster galaxies is not biased with redshift: we find emission in

---

<sup>4</sup> $\Delta(B - V) = 0$  corresponds to  $\Delta(g - r) = 0.26$  according to Equation 3, which is based on GISSEL models, while Yee et al. (1996) give  $\Delta(g - r) = 0.23$  based on the spectral energy distributions of Coleman, Wu, & Weedman (1980).

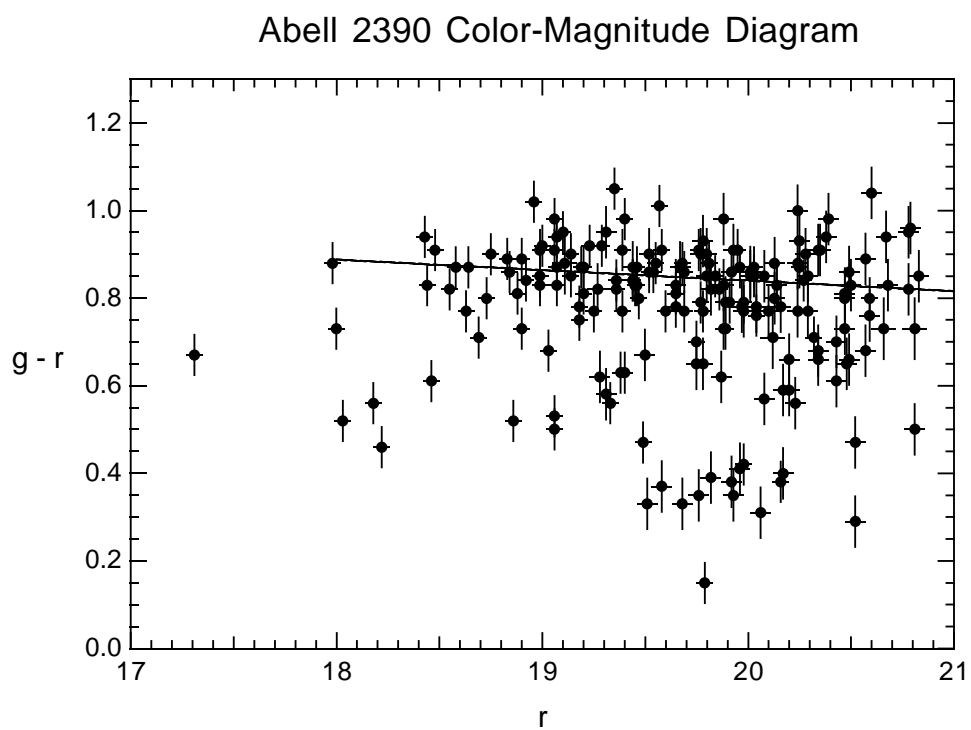


Fig. 5.— Color-magnitude diagram for cluster galaxies. The line is the best fit to the E/S0 color-magnitude relationship of cluster members. See text for details.

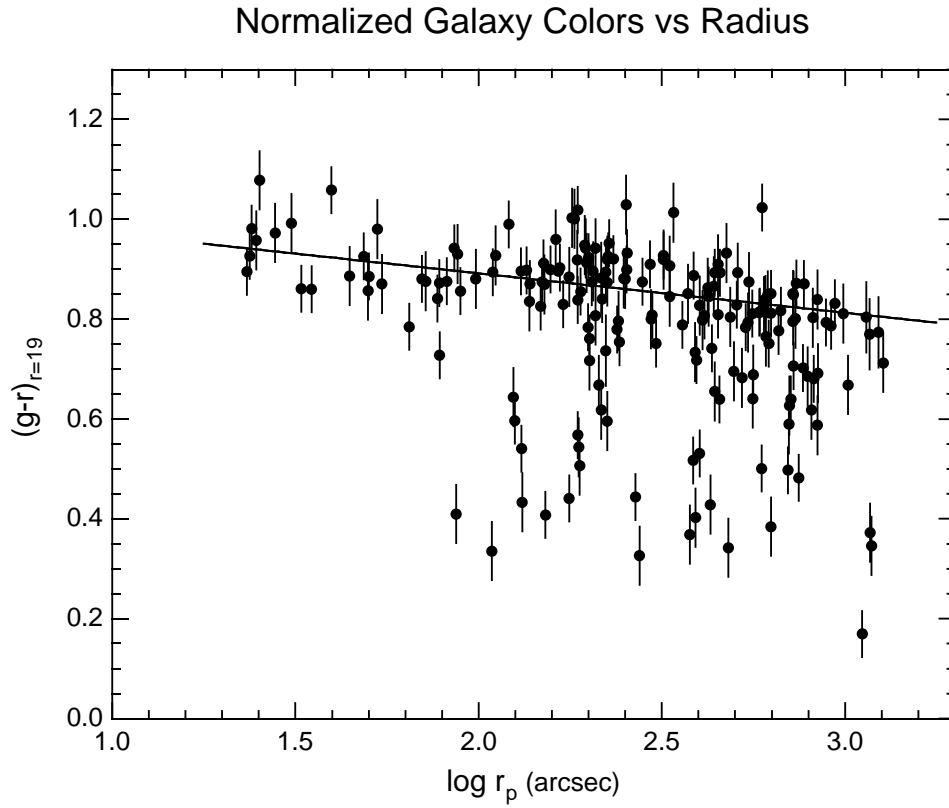


Fig. 6.— The color-projected radius relationship for cluster galaxies where color has been normalized to  $r = 19$  using the color-magnitude relationship. The line is the best fit straight line to the red galaxy locus.

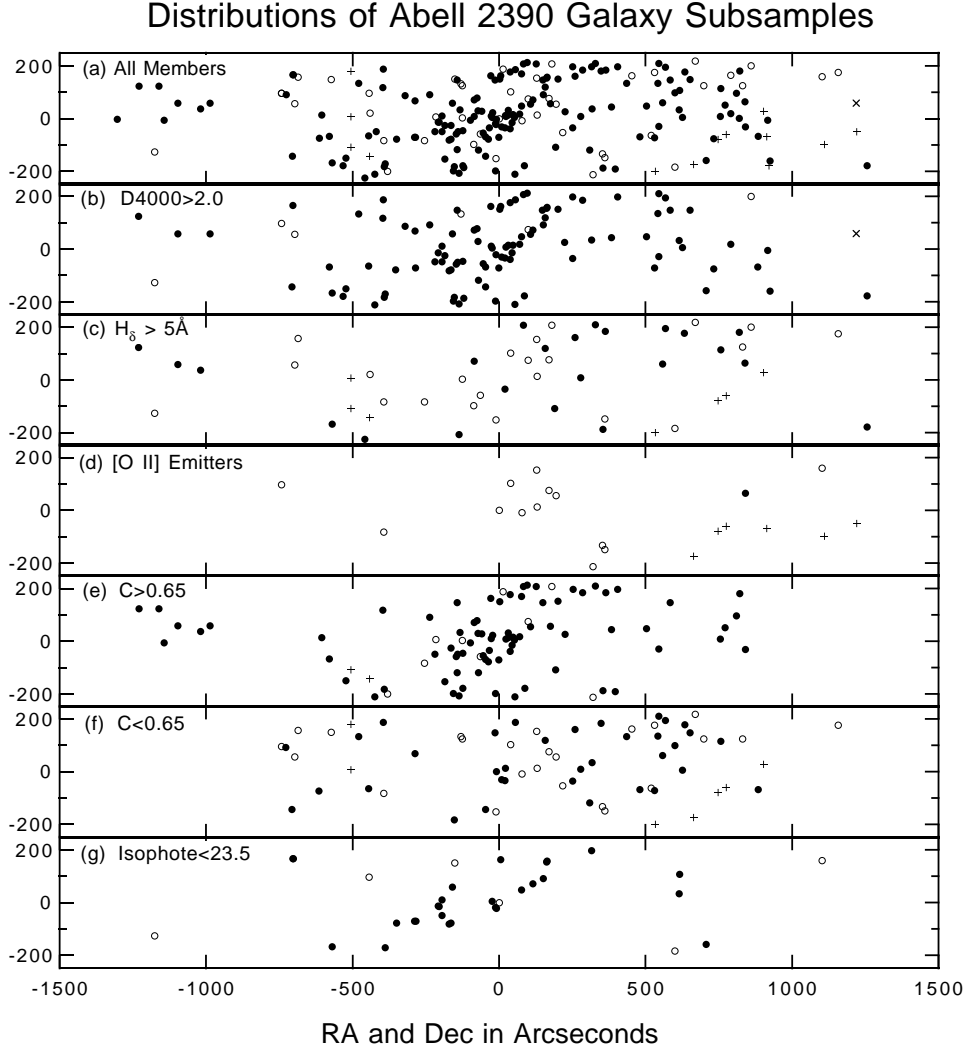


Fig. 7.— The spatial distribution of galaxy subsamples in Abell 2390. Solid circles denote red cluster members, and open circles denote blue cluster members. Red and blue near-field galaxies are denoted by crosses and plus signs, respectively. From top to bottom the panels show: (a) All cluster members and near-field galaxies. (b) Objects with high 4000Å breaks. (c) Galaxies with high  $H\delta$  absorption. (d) Emission line objects. (e) High central concentration galaxies ( $C > 0.65$ ). These galaxies are likely to be early type. (f) Low central concentration galaxies ( $C < 0.65$ ). These are likely to be late type. (g) Galaxies with limiting isophotes brighter than 24 mag/arcsec<sup>2</sup>, as determined by FOCAS. These galaxies have nearby companions or morphological distortions preventing the clean separation of image components.

similar numbers of cluster members with redshifts below and above  $z = 0.228$  (six and eight objects, respectively).

The spatial distribution of [O II] emitters in the cluster is remarkably non-uniform. Eleven cluster members and six near-field objects are on the West side of the cluster, versus two cluster members and no near-field objects on the East side. This 17:2 West/East discrepancy in the positions of cluster and near field line-emitters is not due to uneven sampling on either side of the cluster. In the field, eight [O II] emitters are on the West side of the cluster, versus 6 [O II] emitters on the East side. The distribution of non-[O II]-emitting galaxies is also fairly uniform: 102 members, ten near field objects, and 29 field galaxies line on the West side of the cluster, versus 95 members, four near-field objects, and 26 field galaxies on the East side.

More meaningful counts can be determined by weighting objects by the geometric sampling factor  $W_{xy}$ , given in Yee et al. (1996), which is simply the inverse of the geometric selection function at the position of each galaxy. This factor accounts for biases in slit placement due to local crowding in the slit positions, as well as for differences in the relative number of masks used to obtain spectra across the face of the cluster (the easternmost field had only one mask, whereas the westernmost field had two). Incorporating these geometric weights does not result in a significant change in the West/East bias amongst line-emitters: 17.71 cluster and near-field galaxies lie on the West side of the cluster, versus 1.39 galaxies on the East side. The changes also remain small in the control sample of field [O II] emitters (6.84 objects lie to the West of the cluster center, versus 7.66 objects to the East) and non-[O II] emitters (109.42/10.06/29.94 to the West of the cluster center, versus 94.85/2.97/26.64 objects to the East, amongst members/near-field/field galaxies).

Fig. 8.— Montage of spectra from different types and subsets of galaxies in A2390. Each panel is the sum of 8 – 10 representative spectra of  $S/N > 6$ . The principal line features are identified and all wavelengths correspond to  $z=0.228$ . The left side shows evolved populations, including the NW Group (from top to bottom, parent groups are D4000  $> 2.2$ ; central 19 galaxies; NW group of 23). The right side shows younger populations, selected by  $H\delta$  absorption ( $> 4\text{\AA}$ ) and color ( $g - r < 0.67$ ,  $H\delta < 2$ ). Also shown are summed field galaxies ( $0.27 < z < 0.33$ ), which have similar young population and blue color. The field galaxy spectrum is truncated at red wavelengths because of the shifting required to bring field objects into the cluster rest frame.

### 4.3. $H\delta$ -Strong Galaxies

$H\delta$  absorption with an equivalent width greater than  $5\text{\AA}$  was detected in 45 galaxies (23% of the cluster sample). The distribution of these objects is shown in panel (c) of Figure 7, and is centrally concentrated, although objects with  $H\delta > 5\text{\AA}$  are scarce near the very center of the cluster ( $r_p < 100''$ ). Twenty-two of these objects are blue and are likely to be late-type systems. The remaining 23 objects (12% of the cluster sample) have abnormally strong  $H\delta$  for their colors, and are classified as “HDS systems”<sup>5</sup>.

The  $H\delta > 5\text{\AA}$  criterion used in the definitions of the HDS sample has been chosen rather conservatively because of the comparatively low signal-to-noise level of the spectra in the present sample. In Section 6.2 it is shown that models for  $H\delta$  evolution predict  $H\delta \sim 1\text{\AA}$  for highly evolved early-type systems, and that  $\sim 35$  evolved objects have  $2\text{\AA} < H\delta < 5\text{\AA}$ . Many of these objects are likely to be HDS systems. However, measurements of  $H\delta$  in the present sample have typical uncertainties of  $\sim 2\text{\AA}$ , and reliable classifications of *individual* objects in the  $2\text{\AA} < H\delta < 5\text{\AA}$  regime cannot be made (although statistical comparisons between the distribution of these galaxies and model predictions are meaningful). A fairly crude estimate of the number of HDS systems that are being missed because of low signal-to-noise can be obtained by co-adding subsamples of low signal-to-noise spectra. These spectra were first shifted to the same arbitrary wavelength (0.2280) before being summed (Figure 8). The summed spectra shown in this figure were generally composed of 5 to 10 spectra of  $S/N > 6$ , individually inspected for flaws, and of approximately equal signal. The co-added spectra suggest that a significant fraction (around half) of the red galaxies in the  $2\text{\AA} < H\delta < 5\text{\AA}$  regime are HDS systems. However, co-adding spectra is a procedure subject to many possible systematic errors, and this exercise should only be regarded as providing a rough upper limit of  $\sim 20\%$  to the fraction of HDS systems in the cluster. Therefore the HDS fraction in Abell 2390 is estimated to be 12-20%.

## 5. GALAXY POPULATION MODELS

In order to investigate the nature of the galaxy population in Abell 2390, GISSEL was used to model the evolution of galaxy spectra and colors. A Scalo (1986) initial mass function (IMF) was assumed, with a stellar mass range from  $0.1 M_\odot$  to  $65 M_\odot$ . The results

---

<sup>5</sup>Note that the taxonomy used to denote these objects can be somewhat confusing, since blue objects with  $H\delta > 5\text{\AA}$  in the present sample certainly have strong  $H\delta$  absorption. However, the  $H\delta$  absorption in these objects is not *abnormally* strong for their color, and hence these galaxies are not classified as HDS systems.



vary only slightly with different IMF choices, except if the IMF mass range is severely altered. (A starburst forming only massive stars is shown below as an example.) Colors and D4000 in the observed frame, and equivalent widths in the rest frame, were computed in the same manner as for the observations. The free parameters in our analysis were the star-formation rates and ages of the galaxies, as well as the reddening in the rest frame of the cluster. A foreground Galactic reddening in the direction of Abell 2390 of  $E(B - V) = 0.075 \pm 0.005$  (Burstein & Heiles 1982) was assumed, which corresponds to a foreground reddening of  $E(g - r) = 0.084$  using the calibration of Kent (1985). The possible effects of heavy dust obscuration localized to vigorous star-forming regions (as in IRAS galaxies) have not been modeled. Also, because the GISSEL models are based upon a library of solar metallicity spectra, it is not possible to explore the effects of metallicity. (The effects of metallicity are currently being investigated with Bressan et al. [1994] models.) However, the models of Worthey (1994) have been used to quantify the dependence of color and D4000 on metallicity for elliptical galaxies. In addition, the GISSEL models do not include an HII region component. In star-forming galaxies, Balmer emission from HII regions will increase, and may overwhelm, the stellar Balmer absorption. Therefore, the calculated Balmer absorption equivalent widths for star-forming galaxies should be considered as upper-limits when comparing with real galaxies. The effect of including emission lines on the integrated colors is negligible.

The default definitions of the Gunn  $g$  and  $r$  filters in the GISSEL filter list have been used. These are based on the total transmission of the Palomar 5m telescope + Gunn filters + TI CCD. However, the GISSEL code computes the color zero points using an A0 V star spectrum whereas the zero point of the Gunn photometric system is an F star. Therefore, an additional zero point is required to put the GISSEL  $g - r$  colors on the standard Gunn system. This zero point was calculated by taking the absolute fluxes of a GISSEL 14 Gyr E model and running them through a program which computes colors on the standard Gunn system. The resulting additional zero point in  $g - r$  is  $-0.455$  mag, which is added to the GISSEL colors computed with the default filter definitions. Because the  $g$  filter used for the observations corresponds to the Thuan-Gunn  $g$  band (which has a central wavelength  $\sim 200\text{\AA}$  bluer than the “standard” Gunn  $g$  transmission curve assumed by GISSEL), additional systematic color terms up to  $\sim 0.1$  mag may be present in the  $g - r$  colors.

For  $q_0 = 0.5$  and  $H_0 = 50 \text{ km s}^{-1} \text{ Mpc}^{-1}$ ,  $z = 0.23$  corresponds to  $t_0 = 10$  Gyr and to a look-back time of 3 Gyr. The star-formation rate of a nominal elliptical galaxy (E) was modeled as a burst with a constant rate of star formation lasting for 1 Gyr. The nominal spiral model (S) assumes a constant star-formation rate for 10 Gyr.

In order to compare the colors of field galaxies with our cluster sample, GISSEL models

were used to derive the following relative K-correction in order to convert an observed color  $(g - r)_z$  at  $z$  to  $(g - r)$  at the fiducial redshift of  $z = 0.23$ :

$$(g - r) = (g - r)_z - 2.85(z - 0.23). \quad (2)$$

This correction is valid to within 0.05 mag in  $g - r$  for all galaxy types between  $0.17 \leq z \leq 0.37$ , the range of our field galaxies. To compare with work done on local galaxies, models were also used to derive the following relationship between  $B - V$  measured in the rest frame and  $g - r$  in the observed  $z = 0.23$  frame:

$$(B - V) = 0.20 + 0.77(g - r) \quad (3)$$

which is valid for both E and S SEDs, and

$$B = \begin{cases} 0.56 + 1.00g + 0.63(g - r), & \text{E SED} \\ 0.52 + 1.04g + 0.38(g - r), & \text{S SED.} \end{cases}$$

### 5.1. Checking the predictions of the GISSEL E model

Unfortunately, the observed spectra in the present sample do not extend to  $r$  wavelengths, and hence these spectra cannot be used to test the robustness of the predicted colors. However, to check the prediction of the GISSEL E model a synthetic 14 Gyr E spectrum was compared with a high signal-to-noise spectrum of NGC 4889 (Oke, Gunn, & Hoessel 1995, in preparation), one of the brightest members of the Coma cluster. The comparison of the spectra redshifted to  $z = 0.23$  is plotted in Figure 9. For reference, this figure also shows the Gunn filter transmission curves used by GISSEL. The differences in the spectra are relatively small, and the computed  $g - r$  color of the model at  $z = 0.23$  is 0.08 mag *bluer* than the NGC 4889 spectrum. The observed NGC 4889 spectrum is extremely well calibrated, but it was obtained through a narrow slit. Because galaxies do have internal gradients, a spectrum integrated over the entire galaxy, as is the case for our A2390 data, may show somewhat different spectral energy distribution. Therefore, the GISSEL model was also compared against an NGC 4889 spectrum taken through a wide aperture (Kennicutt 1992). Redshifted to  $z = 0.23$ , the model is 0.09 mag *redder* in  $g - r$  than the Kennicutt spectrum of NGC 4889. However, Kennicutt cautions that the data may have  $\sim 10\%$  uncertainties in the photometric calibration over the wavelength range of interest. The GISSEL models therefore appear to predict the spectra and color of local elliptical galaxies fairly well, with discrepancies in color  $\lesssim 0.10$  mag.

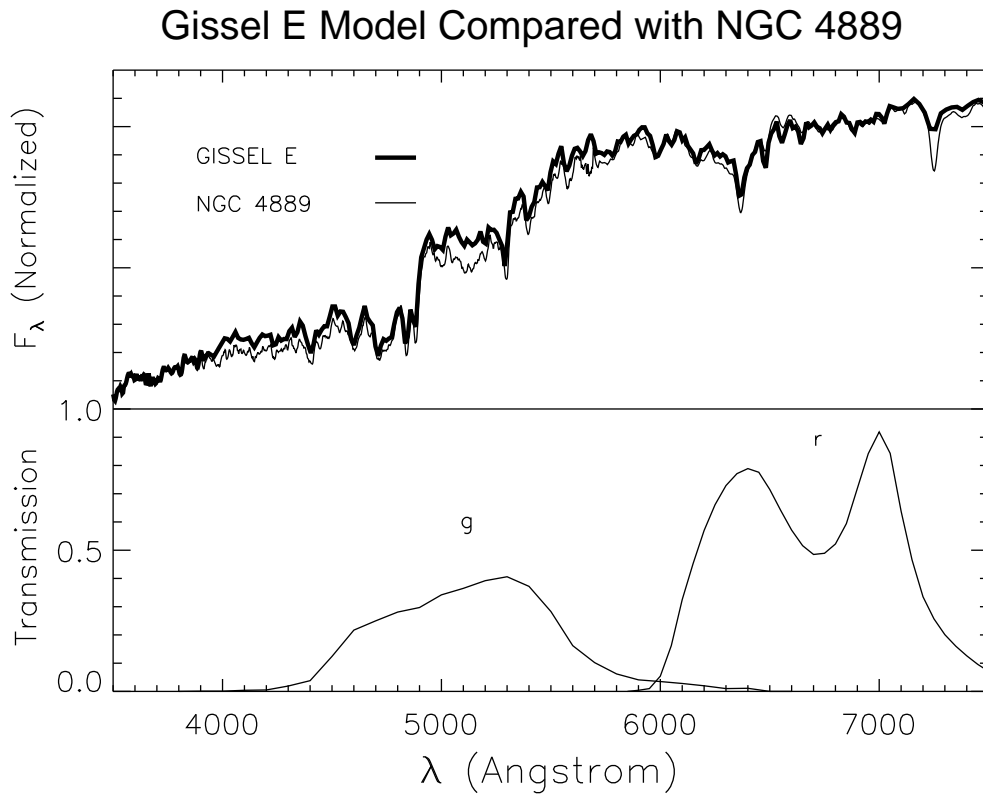


Fig. 9.— Upper: Comparison of the GISSSEL 14 Gyr E model (thick line) with a spectrum of NGC 4889 (thin line). Lower: the Gunn *g* and *r* filter transmission curves used by GISSSEL.

## 6. COMPARISON OF DATA AND MODELS

There are clear radial gradients in the colors, spectroscopic properties and morphologies of the galaxies in Abell 2390 (Figure 10). Consequently the GISSEL models will be compared to the data in radial bins. A successful model must account for the following key observations:

- (1) The almost complete absence of blue galaxies within the central 100'' of the cluster.
- (2) The color gradient in the red galaxy sequence as a function of radius.
- (3) The relative increase in the blue fraction, and the increased blueness of the bluest galaxies, as a function of radius.
- (4) The large radial extent of the dominant red galaxy sequence in the cluster.
- (5) The nature of the many cluster members seen at large radii whose colors and spectral indices are intermediate between those expected for E/S0s and normal spirals (eg. the HDS galaxies).

Explaining these observations with spectral synthesis models can be rather complicated since age, metallicity and reddening may all be important. Color data alone are inadequate for testing models. For example, a model of an elliptical galaxy (constant star-formation rate for  $t \leq 1$  Gyr, solar metallicity) reddens by  $\Delta(g - r) = 0.1$  between the age of 3.5 and 10 Gyr (Bruzual & Charlot 1993). The same amount of reddening is predicted for 10 Gyr old ellipticals if the mean metallicity changes from  $[\text{Fe}/\text{H}] = 0$  to  $+0.25$  (Worthey 1994). The 4000 Å break, D4000, can also be used as an age indicator but it too is sensitive to metallicity in old stellar populations. Although Dressler & Schectman (1987) found only a weak correlation between absolute magnitude (*i.e.*, metallicity) and D4000 in E/S0 galaxies, more recent studies of field and cluster E/S0 galaxies over a wider range of absolute magnitude find a significant correlation (Kimble et al. 1989, Davidge & Clarke 1994). In their data, Kimble et al. (1989) find that D4000 correlates well with a variety of metallicity indicators in the sense that galaxies with smaller D4000 (fainter  $M_B$ ) have weaker metal lines. Although D4000 is systematically lower for galaxies with [O II] emission, indicative of current star-formation, the bulk of the trend appears to be more correlated with the strength of the metal absorption lines. However, for the bright end of the luminosity function ( $-22 \leq M_B \leq -19$ ) the slope of the relationship between D4000 and  $M_B$  is relatively shallow ( $0.03 \text{ mag}^{-1}$ ). Fainter than  $M_B = -19$ , the relationship steepens, and hence metallicity has been inferred to be the primary cause of D4000 variations in E/S0 galaxies fainter than  $M_B = -19$ .

In the present work the star-formation history of cluster members is constrained by

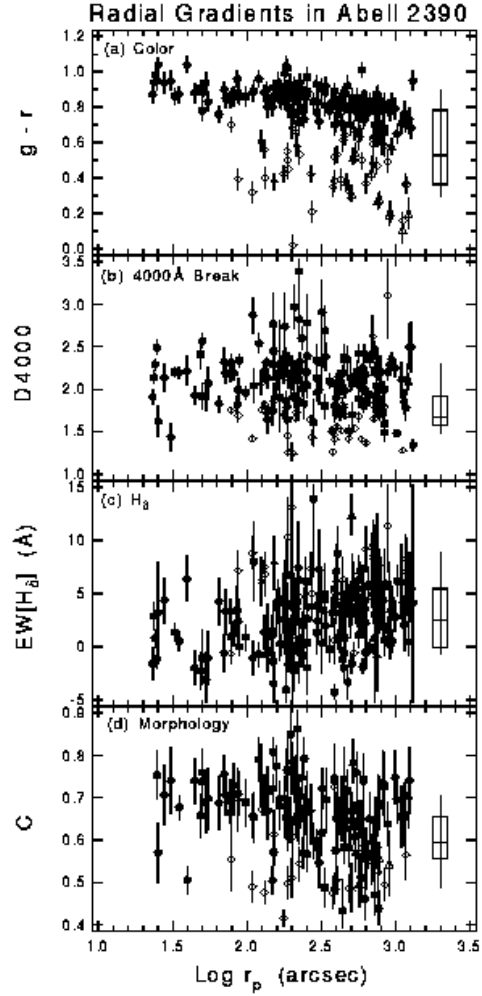


Fig. 10.— The radial gradients in color, line measures, and morphology, plotted as a function of projected radius for our sample of cluster and field galaxies. Filled circles are red cluster members, and open circles are blue cluster members. Similarly, filled triangles are red near-field galaxies, and open triangles are blue near-field objects. Negative values of the line measures correspond to emission. The symbol at the right of each panel is a “Tukey box plot” showing the field distribution. The box encloses the 25th and 75th percentiles for the field sample, and is subdivided by the median. The vertical bar spans the range between the 10th and 90th percentiles of the field distribution. Field galaxy colors have been K-corrected into the cluster rest frame. See text for further details.

using color and D4000 *in unison*, along with measures of Balmer lines (which are mainly sensitive to age), in order to model the observations. These measures will be discussed separately in the following subsections. In the diagrams below the temporal evolution of the E and S models (solid lines) are superposed on the data. Fiducial ages of  $t = 1, 2, 3, 5, 8$  and 10 Gyr are indicated on the models with small dots. To illustrate the radial gradient in the galaxy population, the data has been split into 4 bins defined by projected radius: (a) the inner cluster ( $r_p \leq 100''$ ), (b) the cluster at intermediate radii ( $100'' < r_p \leq 400''$ ), (c) the cluster at outer radii ( $r_p > 400''$ ), and (d) the field. The colors of the field sample have been k-corrected to  $z = 0.23$  using equation 2. Galaxies with [O II] emission detections  $> 2\sigma$  are plotted as open circles.

### 6.1. Color and 4000 Å break

Figures 11 and 12 show D4000 versus color, both for our complete sample and for a subsample of galaxies with high signal-to-noise spectra ( $\text{SNR} > 6$ ). The vector labeled A illustrates the change produced by a reddening of  $E(g-r) = 0.18$  mag ( $A_V = 0.5$  mag) in the rest frame of the cluster for the E model. The vector labeled Z shows the movement of 10 Gyr old elliptical if metallicity varies from  $[\text{Fe}/\text{H}] = 0$  to  $+0.25$  (Worthey 1994).

#### 6.1.1. Inner Cluster Members ( $r_p < 100''$ )

The inner cluster galaxies are in good agreement with the GISSEL models, and have a small color dispersion but moderate dispersion in D4000. This may be caused by either age or metallicity variations. As can be seen from the models, changes in age and metallicity fall along roughly parallel lines, and hence they are inseparable in this plane<sup>6</sup>. In the absence of synchronizing effects, the narrow color dispersion envelope at small radii implies that the galaxies in the inner parts of the cluster have a relatively small age spread (Aragón-Salamanca et al. 1993). We can definitively say that these galaxies have had little star formation in the 3 Gyr prior to the epoch of observation, and only four galaxies can be significantly younger than 5 Gyr. Assuming that their epoch of star formation lasted  $\sim 1$  Gyr and their mean metallicities are approximately solar, the remaining galaxies are

---

<sup>6</sup>However, it is interesting to note that a co-added spectrum of the four innermost cluster galaxies shown in Figure 11 with  $\text{D4000} \approx 1.9$  shows a higher  $\text{H}\delta = 3 \text{ \AA}$  and weaker Ca II K than the co-added spectrum of the inner 12 galaxies with  $\text{D4000} > 2$ . These could be signs of age rather than metallicity differences, but higher S/N data are required in order to investigate this further.

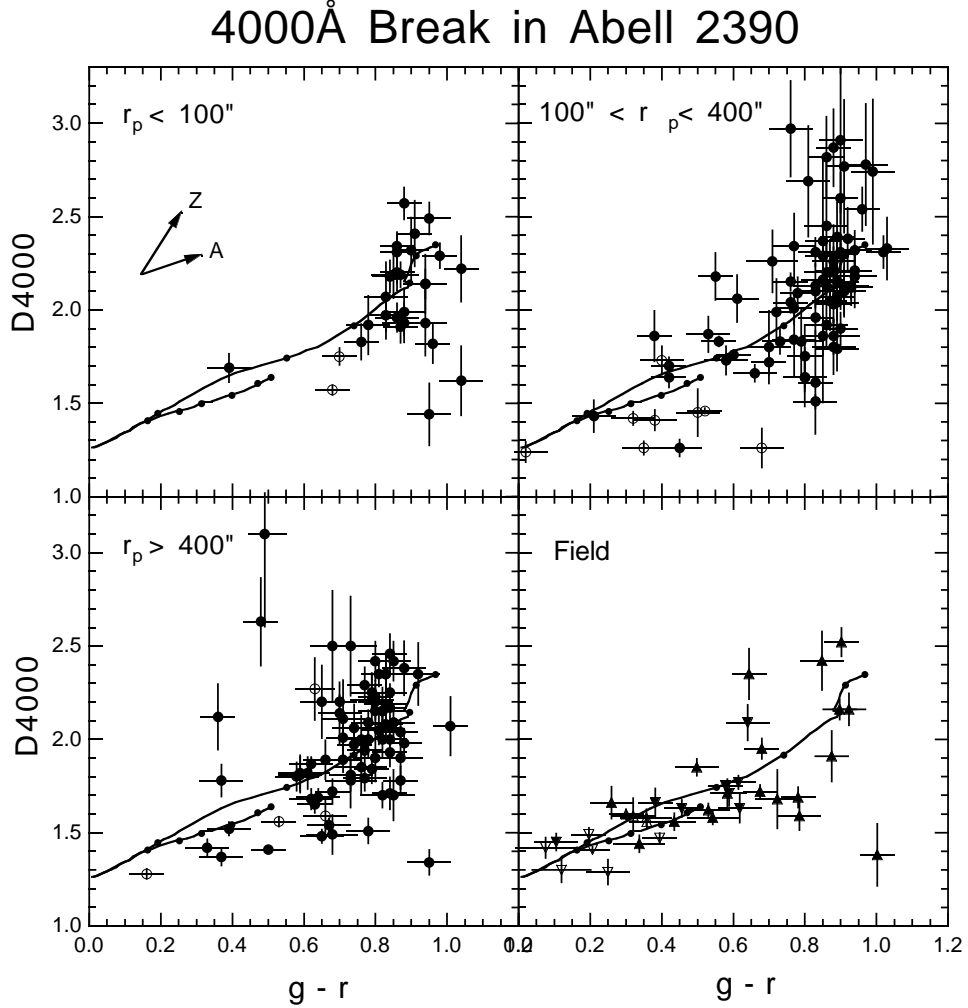


Fig. 11.— D4000 vs color for galaxies in the cluster and field for different bins of projected radius. The Z vectors show the effects of changing  $[\text{Fe}/\text{H}]$  in an old elliptical from 0 to +0.25. The A vector shows the change produced by a reddening of  $E(g-r) = 0.18$  mag ( $A_V = 0.5$  mag) in the rest frame of the cluster for the elliptical model (see text for details). Open symbols denote galaxies with  $2\sigma$  detections of  $[\text{O II}]$  emission. In the field galaxy panel redshifts have been limited to  $0.17 < z < 0.39$  in order to correspond to the regime where K-corrections can be estimated accurately. Upward-facing triangles are field objects, and downward facing triangles are near-field objects. The temporal evolution of the E and S models are shown as solid lines, and ages  $t = 1, 2, 3, 5, 8$  and 10 Gyr are identified with small filled circles.

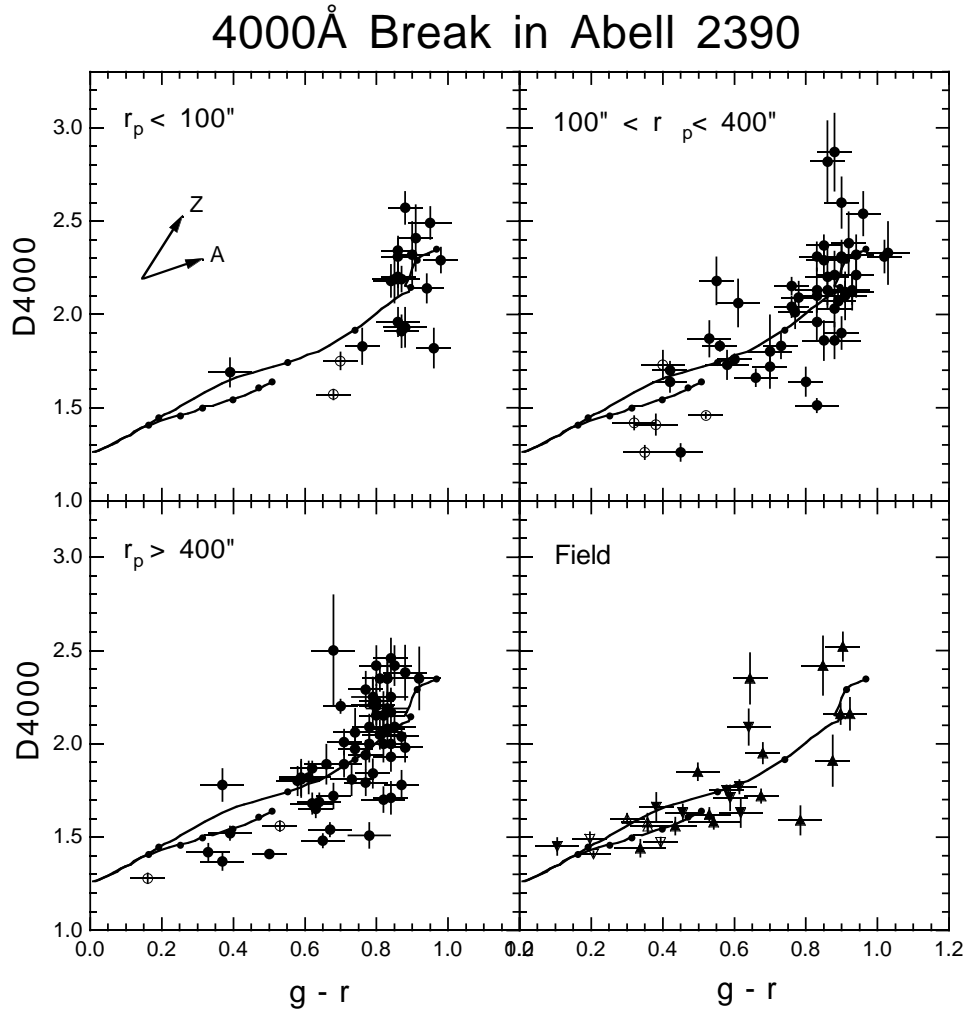


Fig. 12.— As for the previous figure, except that the sample has been restricted to objects with high signal-to-noise level ( $\text{SNR} > 6$ ) spectra.



consistent with being coeval with ages =  $8 \pm 2$  Gyr at  $z = 0.23$ . Thus their redshift of formation is large,  $z_f \geq 2$ , and they must have formed early during the initial collapse of the cluster. Although the dispersion in D4000 that is seen in the central galaxies is larger than expected based on their absolute magnitude range, we cannot conclude that this represents a dispersion in age or metallicity because we may have additional systematic errors in D4000 due to uncertainties in flux calibration of the slitlets.

### 6.1.2. Outer Cluster Members ( $r_p > 100''$ )

Outside  $r_p = 100''$  the models remain in good agreement with the D4000 and color data. The galaxies occupy the regions predicted for star-forming galaxies (S model), and along the passively evolving E model. *The galaxies apparently track an age sequence*, and the agreement with the models is excellent because D4000 is much more sensitive to age than to metallicity for young stellar populations. Galaxies bluer than  $g - r = 0.4$  lie near or on the S track and have active star-formation (low D4000, [O II] emission). Objects with  $0.5 < g - r < 0.7$  correspond to systems in which star-formation has ceased (we will show in the next section that these systems generally have strong Balmer absorption), and consequently D4000 is higher. The reddest galaxies correspond to progressively older, passively evolving populations and occupy the same position in the D4000-color plane as the inner objects with  $r_p < 100''$ . Outside the cluster, the field population is in excellent agreement with the predictions of the model (90% of the galaxies lie on or near the S track or the young part of the E track).

## 6.2. H $\delta$ Evolution

In Figures 13 and 14 H $\delta$  vs color is shown using same bins of projected radius adopted for the D4000 plots. As with the previous figures, the nominal E and S models have been superposed on the data. There is excellent agreement between the models and observations for galaxies in the field. The agreement is also good for objects with radii  $r_p < 100''$ . This is not true for objects at intermediate radii ( $r_p > 100''$ ): either H $\delta$  is too strong, galaxies are too red, or some combination of both of these effects is occurring. These objects (the most striking of which have already been discussed in Section 4.3) apparently correspond to the HDS (and E+A) systems found by Dressler & Gunn (1983) and Couch & Sharples (1987) in their cluster surveys.

In order to investigate the nature of these HDS systems, GISSEL was used to compute

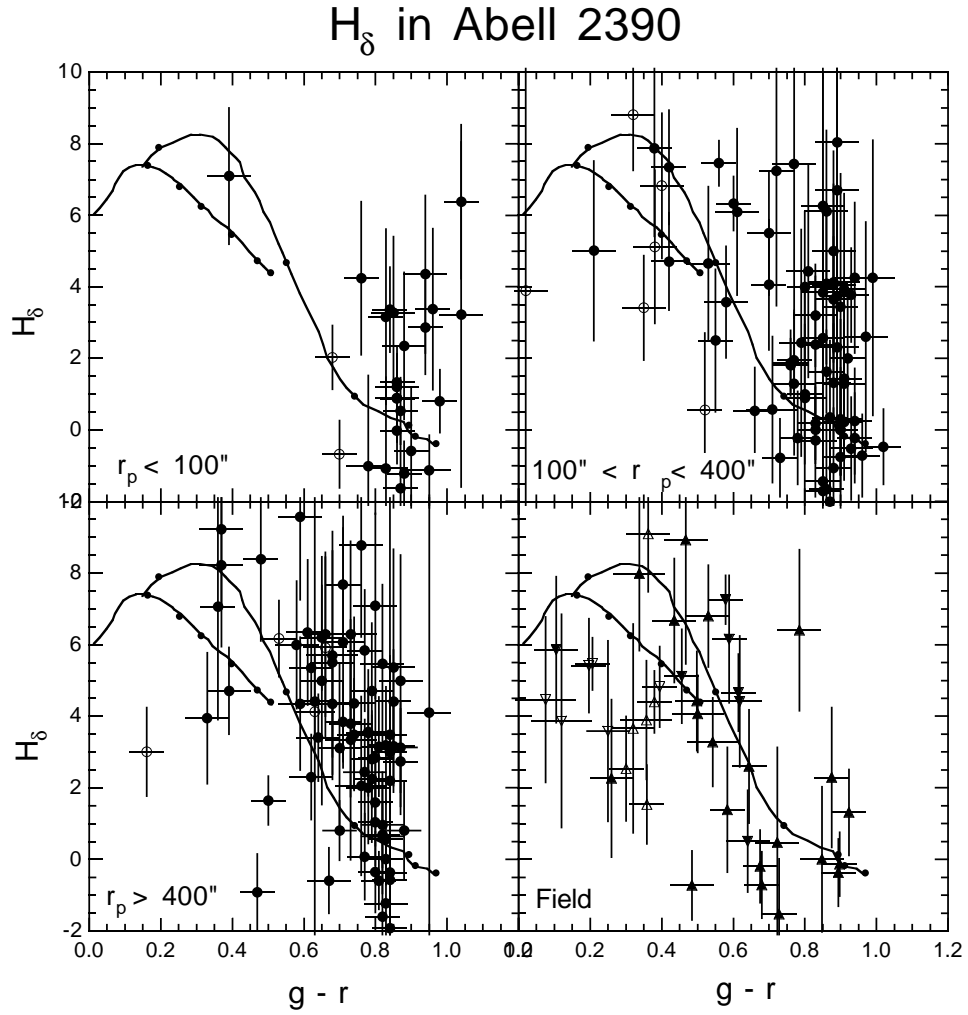


Fig. 13.— Equivalent width of H $\delta$  vs color for (a–c) cluster members in bins of projected radius  $r_p$  (as for previous figure), and (d) field galaxies. Solid lines are the nominal E and S models. The plot symbols have the same meaning as for the previous figure.

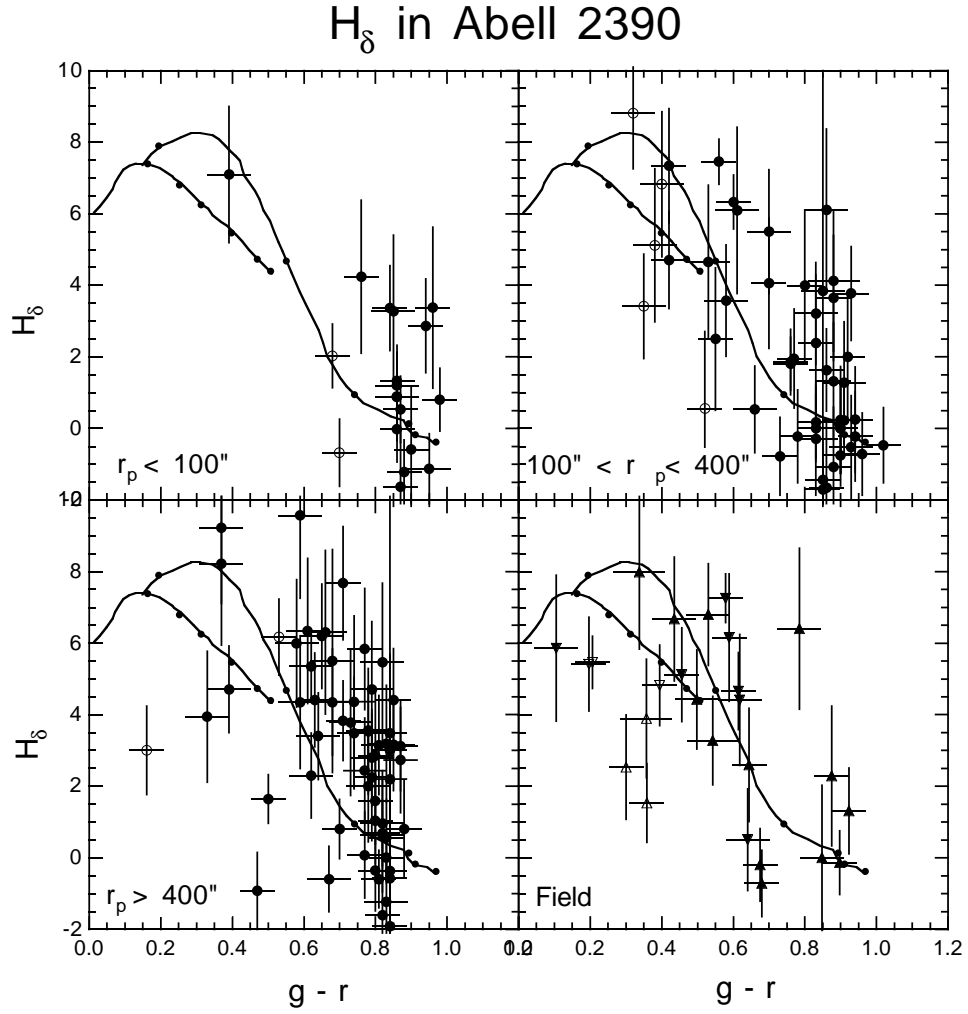


Fig. 14.— As for the previous figure, except that the sample has been restricted to objects with high signal-to-noise level ( $\text{SNR} > 6$ ) spectra.

the evolutionary tracks of both starburst and truncated star formation models on the  $H\delta$ -color diagram (Figure 15). In each panel of this Figure the nominal E and S models have been displayed as a benchmark. In panel (a) the positions corresponding to passively evolving galaxies with ages  $t = 1, 2, 3, 5, 8$  and 10 Gyr are indicated. Panel (b) shows two truncated star-formation models in which the nominal S is truncated at  $T = 3$  and 8 Gyr, and ages  $t = T + [0, 0.5, 1, 1.5, 2]$  Gyr are marked. Panel (c) shows two models of star bursts in an E galaxy which form 10 and 20% of the total mass of stars formed in the galaxy. The bursts are assumed to begin at  $T = 8$  Gyr and last 1 Gyr. The ages marked are the same as in (b). Panel (d) shows the identical two bursts in an S galaxy. *In each starburst model, we assume that star formation ceases after the burst.* Figure 16 shows the same S + starburst model under the assumption that IMF in the burst is biased to form only massive stars (2.5 to 125  $M_{\odot}$ ). The observed distribution of HDS objects on the  $H\delta$ -color diagram is in qualitatively good agreement with the evolutionary tracks shown in Figures 15 and 16. However, the observed  $H\delta$  values tend to be somewhat larger than predicted by the both starburst and simple truncated star formation spectral synthesis models. Models with IMFs biased toward massive stars reproduce a steep  $H\delta$  vs  $g - r$  as seen in the data, but the steepness of the  $H\delta$  points may also be produced by factors such as temporal variations in internal reddening in truncated or burst models, or by changes in metallicity. These factors are not accounted for in the GISSEL models.

It is apparent from Figures 15 and 16 that the behavior of  $H\delta$  can be qualitatively understood as the manifestation of a *halt in star formation*. The key question to be addressed is whether or not this halt is due to (a) the resumption of ordinary behavior in ellipticals that have undergone bursts (the original E+A scenario proposed by Dressler & Gunn 1983), (b) exhaustion in the gas supply of disk systems that have undergone starbursts (favored by Couch & Sharples 1987), or (c) truncation in the star formation rates of ordinary (i.e. non-bursting) disk systems. However, once galaxies have reached the HDS stage the shapes of the evolutionary tracks for all these scenarios are rather similar. In the starburst model  $H\delta$  (as well as color and D4000) declines on a timescale  $\sim 2$  Gyr after the burst has ceased, irregardless of whether the initial galaxy is a S or E. After the burst, the E + burst model is only slightly redder than the the S + burst model. Given the relatively large uncertainty in our  $H\delta$  measurements the later evolutionary stages of the burst and truncated star-formation tracks are effectively indistinguishable. Therefore the key observable quantity in our data that can be used to discriminate between starburst and simple truncated star formation scenarios is the fraction of galaxies at early points on the evolutionary tracks versus the number of potential post-starburst systems (ie. the number of systems currently undergoing starbursts versus the number of HDS galaxies).

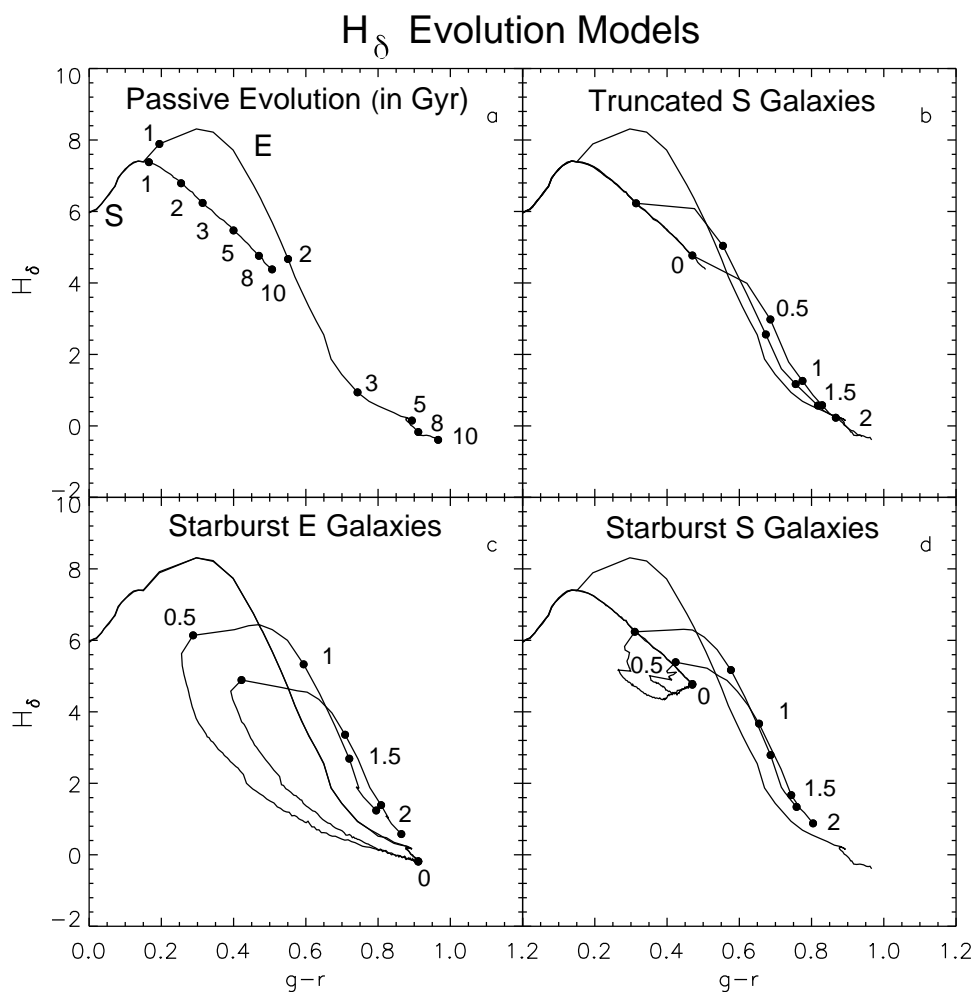


Fig. 15.— Models of H $\delta$  evolution: (a) Nominal E and S model. The numbers correspond to age in Gyr. (b) Truncated S models. The numbers correspond to time (in Gyr) after the onset of truncation. (c) star bursts in the E model, and d) star bursts in the S model. Numbers correspond to time (in Gyr) after the burst. See text for more details.

## Starburst with Truncated IMF

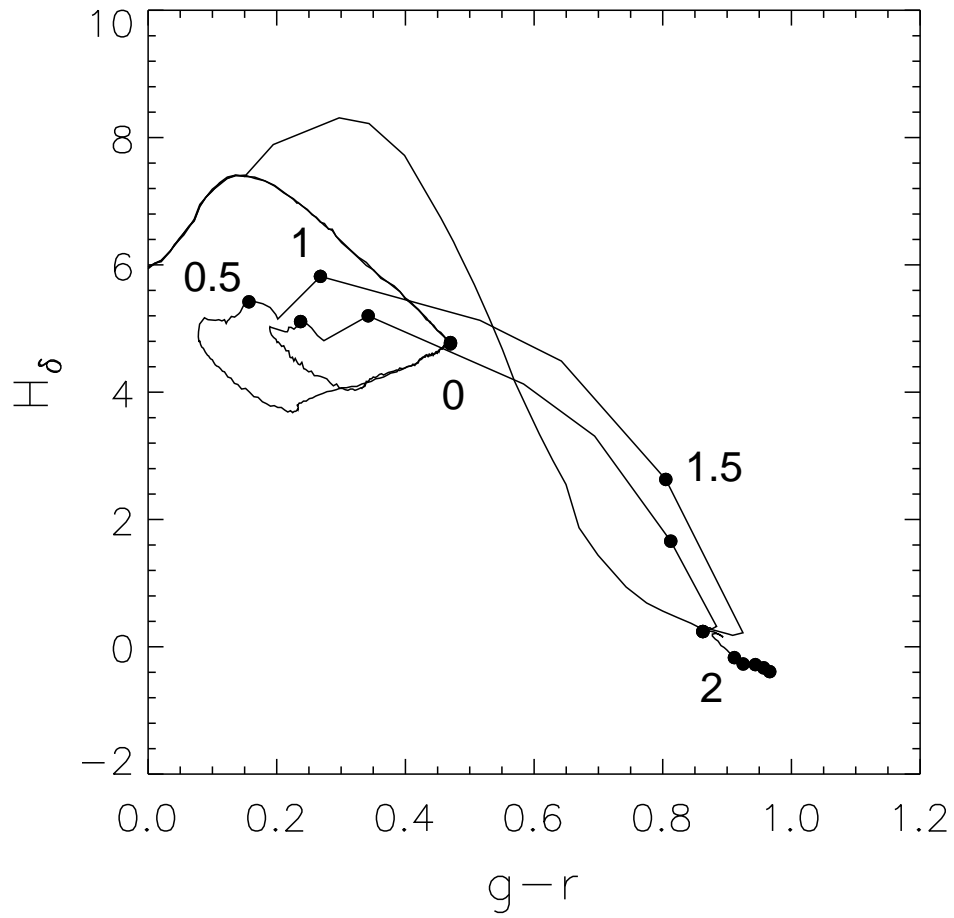


Fig. 16.— Model of  $H\delta$  evolution: a star burst in the nominal S model with a truncated IMF that forms only massive stars (2.5 to 125  $M_{\odot}$ ). Numbers on the tracks correspond to time (in Gyr) after the burst.

### 6.3. The starbursting fraction

The equivalent widths and rest-frame colors of cluster and near-field galaxies with [O II] emission detected at the  $2\sigma$  level are shown in Figure 17. Equation 3 has been used to convert observed  $g - r$  to rest frame  $B - V$ . The trapezoid superposed on the points corresponds to the region occupied by nearby cluster and field galaxies with ordinary emission line characteristics (Dressler & Gunn 1982). In local galaxy samples, Sbc's typically have  $B - V \approx 0.58$  mag and [O II]  $\approx 10\text{\AA}$ , Scds have  $B - V \approx 0.48$  mag and [O II]  $\approx 17\text{\AA}$ , and Ims have  $B - V \approx 0.48$  mag and [O II]  $\approx 48\text{\AA}$  (Coleman, Wu & Weedman 1980, Kennicutt 1992). In the Abell 2390 sample of fourteen cluster members with detected [O II] emission at the  $2\sigma$  level, six galaxies appear to be normal spirals, three are either normal spirals or galaxies with star formation rates slightly (a factor of  $\sim 2$ ) higher than normal, and five objects (only 2% of the total cluster population) are starburst/AGN candidates. Amongst the six near-field [O II] emitters, five objects are consistent with being late-type systems, and one galaxy is probably a starburst. The properties of the individual starbursting systems in our sample are described in §7.4.

## 7. Discussion

### 7.1. Truncated star formation

On the basis of Figures 13 – 17 one can immediately rule out the possibility that galaxy evolution in clusters is a *continuous* process proceeding via starbursts. Our observations rule out the possibility that large numbers of starbursts are currently occurring. Furthermore, the relative number of galaxies at different positions along starburst model evolutionary tracks in Figure 15 rules out the possibility that *steady* evolution in the galaxy population occurred via starbursts in the recent past. Figure 15 indicates that both bursting ellipticals and bursting spirals spend 40–45% of the first 1.5 Gyr following a starburst blueward of the passive evolution elliptical curve before looping across and joining the elliptical curve  $\gtrsim 2$  Gyr after the burst. However, in the data shown in Figures 13 and 14 only 15–20% of the galaxies lie blueward of the passive evolution track in the region of the diagram corresponding to times between 0 and 1.5 Gyr following a burst. Therefore the majority of the HDS population must have evolved via truncated star formation *that did not follow from an initial starburst*. Furthermore, because of the selection criteria in the present sample, the fraction of non-burst HDS galaxies determined on the basis of relative position along the tracks in Figure 15 is likely to be significantly underestimated. Bursting galaxies (and post-starburst galaxies blueward of the passive evolution tracks) have been brightened,

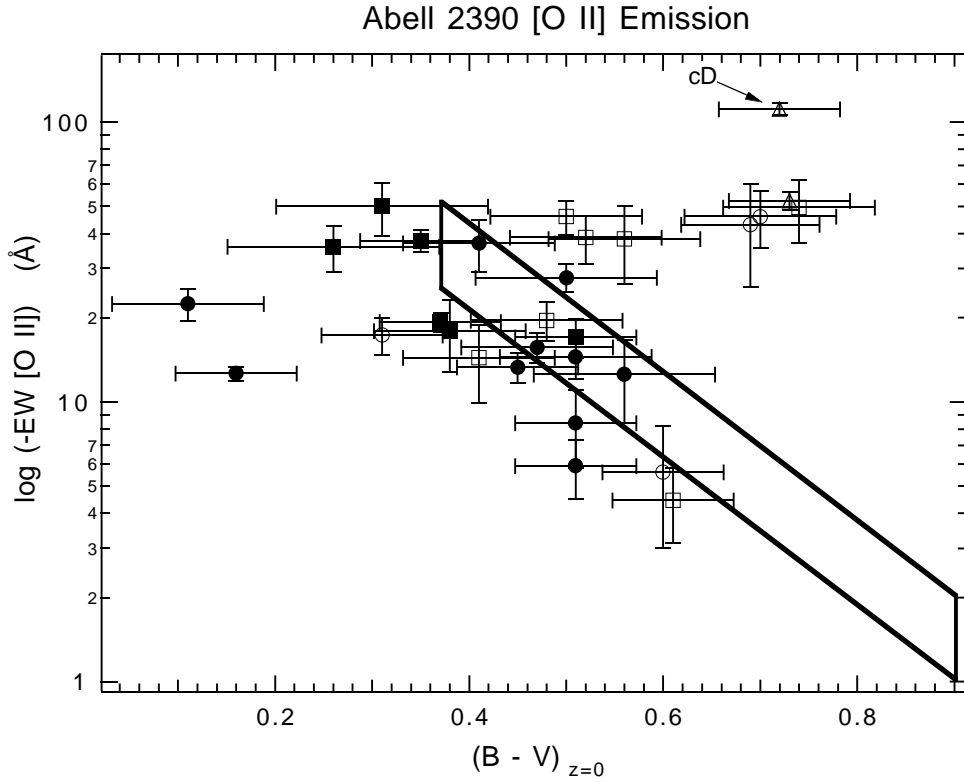


Fig. 17.— The equivalent widths of [O II] 3727 in galaxies with  $> 2\sigma$  detections: triangles are inner cluster members ( $r_p \leq 100$ ), squares are cluster members at intermediate radii ( $100 < r_p \leq 400$ ), circles are cluster members at large radii ( $r_p > 400$ ), filled squares are near-field galaxies and filled circles are field galaxies. The trapezoid represents the area occupied by a sample of nearby cluster and field galaxies Dressler (1982).



while HDS objects redward of the passive evolution tracks have faded. The magnitude selection function for the present sample is falling rapidly near  $r = 21$  mag, and intrinsically less luminous objects are under-represented.

The argument given above suggests that if wholesale changes in the cluster galaxy population have been precipitated by starbursts, then such changes must have been episodic, with the last period of starbursts ending about 1 Gyr before the epoch of observation. Episodic bursts are difficult to constrain from spectral synthesis models, since one can always argue that at the epoch of observation the cluster is no longer evolving in the same manner as in the past. However, if the galaxies in Abell 2390 form a radial sequence as we postulate, and if episodic starbursts are triggered by specific environmental conditions, then it seems reasonable to argue that at *some* radius galaxy evolution via starbursts should be occurring. The large radial coverage in the present dataset effectively rules this out. Furthermore, if episodic starbursts (rather than steady evolution) dominate the evolutionary process in clusters, then one expects to see a large scatter in the cluster blue fraction as a function of redshift. Both the results of Butcher & Oemler (1984) and preliminary results from the CNOC survey (Yee et al. 1995) suggest a steady monotonic rise in the cluster blue fraction as a function of redshift.

It is therefore suggested that galaxy evolution in Abell 2390 is being driven by the *steady truncation in the star formation rate of infalling galaxies*. In this scenario Abell 2390 is composed of a central red old population, and an outer envelope of progressively younger galaxies which have been accreted from the field over  $\sim 8$  Gyr. It is important to be clear about what is meant by “younger” galaxies in this context, since age can be measured either in terms of time since the initial onset of star formation or in terms of the mean age of the stellar population. At a given radius the slope of the red galaxy locus on the color-radius diagram implies that (on average) the *oldest* galaxies at that radius *ceased forming stars* more recently than did the oldest galaxies nearer to the center of the cluster. However star-formation models do not give unique predictions. One can produce the bluer colors either by starting star formation in the galaxies at later times, having an increase in the star-formation rate at later times, or truncating a constant star-formation rate at later times. We interpret the increased dispersion in the colors of blue galaxies on the color-radius diagram to mean that at larger cluster radii galaxies have had longer periods of star formation before that star formation was halted by infall into the cluster. Hence our claim is also that *the mean age of the stellar population in galaxies becomes younger with increased radius in the cluster*. This dynamical picture of a growing cluster is consistent with hierarchical scenarios for the evolution of large scale structure (Gunn & Gott 1972).

This scenario is also consistent with the remarkable East/West dichotomy in the distribution of line emitters that is seen in Figure 7, and with the bulk motion along the West side of the cluster indicated by the Dressler-Shectman test shown in Figure 1 (and roughly centered on the NW Group). These suggest that Abell 2390 is accreting objects from the field non-isotropically, perhaps along a “sheet” of large scale structure joined to the West side of the cluster. Some infalling objects may undergo mild starbursts induced by interactions with the ICM, but Figure 17 suggests that most infalling line emitters are simply late-type systems common in the field. Assuming infalling objects have peculiar motions of order  $\sim 1000 \text{ km s}^{-1}$ , accreted galaxies in the periphery of the cluster move one Megaparsec in a Gigayear (the approximate timescale for fading the disk of a field galaxy and turning it into a red HDS system). Since infalling objects fade before completing a single cluster crossing, the spatially skewed color distribution between the cluster and infalling field population on the West side of the cluster is preserved.

It is illustrative to compare directly the observed colors of cluster galaxies with predicted colors as a function of age and duration of star formation prior to truncation (Figure 18). The  $g - r$  colors calculated from the GISSEL package are displayed on the left half of this figure, under the assumption that truncated star-formation has occurred in Abell 2390. The lines, from left to right are for star-formation durations of 1 Gyr to 10 Gyr, at intervals of 1 Gyr. On the right half of Figure 18 histograms indicate the observed color composition in the cluster as a function of radius. The radial bins are identical to those in Figure 11 (a–d from left to right). With a few exceptions, the colors fall into the range predicted by the model. The two galaxies (1% of the total) with bluer colors are entirely consistent with being chance projections of field galaxies. While there are clearly *some* strong [O II] emission line objects in the present cluster sample, these are consistent with being comparatively “minor” starbursts (resulting from the continuous formation of  $\lesssim 20\%$  of the galaxy), and probably do not play a major role in driving cluster galaxy evolution.

## 7.2. Morphological Evolution

The stellar populations (as measured from colors and spectroscopic features) of the cluster members are consistent with a truncated star formation scenario, but a self-consistent model for galaxy evolution in Abell 2390 must not only account for colors and line features, but also for morphological composition. Truncation in the star formation rate must account for a gradual radial evolution in the morphologies of the galaxy population, starting from the late-type-dominated field population, through “anemic” spirals, and leading ultimately to S0 galaxies. Truncated star-formation models for the origin of S0s have been proposed

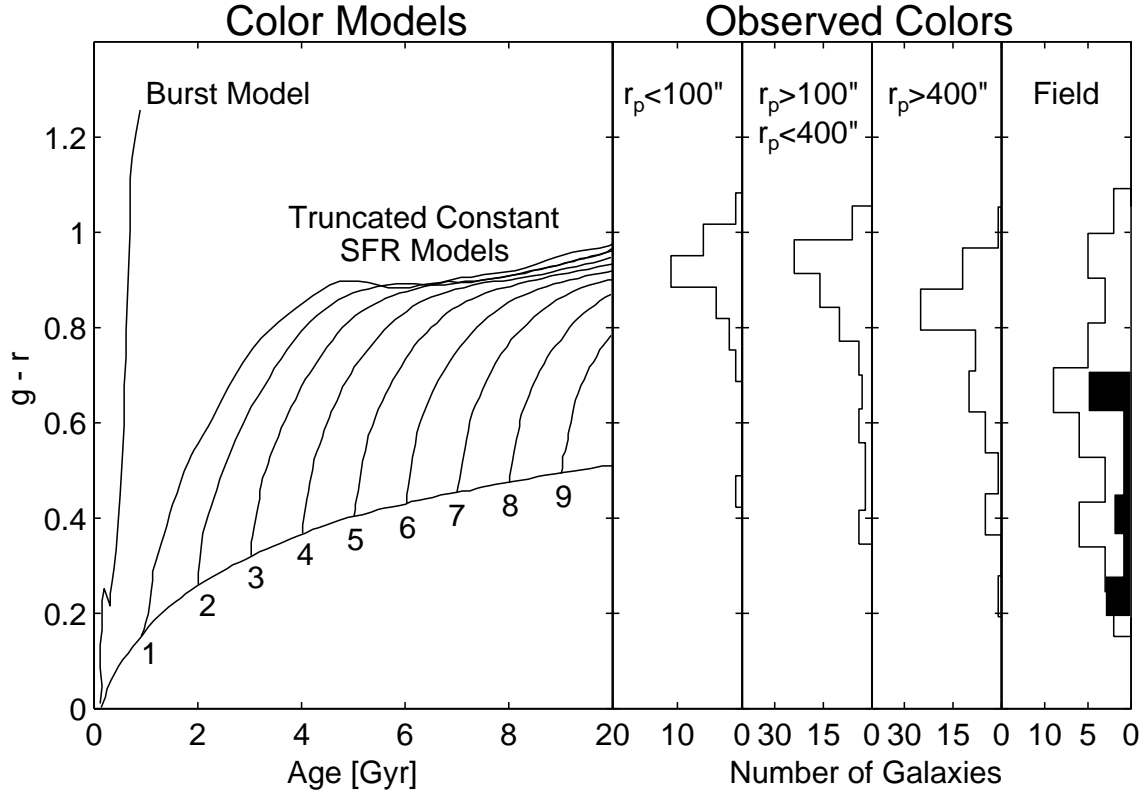


Fig. 18.— Illustration of the agreement between the color models and the observed colors at different radii. [Left] the color-age relation for truncated, constant star-formation rate models. The models are truncated at various ages from 1 to 10 Gyr in 1 Gyr intervals. The short line which peaks at a very red color is a burst model assuming an IMF which is biased to form only massive stars (2.5 to 125  $M_{\odot}$ ). Note that the stars have all evolved to near-maximum redness by  $t \sim 1.5$  Gyr after truncation. [Right] histograms of the colors of galaxies which are (from left to right) inner cluster members, cluster members at intermediate radii, outer cluster members, and field galaxies. The galaxies shown in grey are the near-field galaxies.

many times, and diverse physical mechanisms have been proposed for halting star formation, such as ram-pressure stripping (Gunn & Gott 1972) and gas evaporation (Cowie & Songaila 1977). However, the “Nature vs. Nurture” formation history of S0s remains controversial (see Haynes 1988 for a review). A major objection to an evolutionary linkage between spirals and S0’s appears to have been eliminated by the work by Solanes, Salvador-Solé, & Sanromà (1989) showing that the increase in the disk-to-bulge ratio of spirals in denser regions (seen in the Dressler [1980] data) is due to a diminution of disk luminosity, rather than an increase in bulge luminosity as originally thought.

To examine the effects of truncated star formation on morphology, GISSEL models were used to compute separately the expected fading in the disk and bulge components of late-type systems at  $z \sim 0.25$ . As before, disks were modeled using a constant star-formation rate. Bulges were modeled in the same manner as for elliptical galaxies (a constant star-formation rate for 1 Gyr). Assuming a Scalo (1986) IMF and an age for the composite system of 7 Gyr, one Gyr after truncating the star formation a typical disk has faded by  $\sim 1$  mag, while the bulge component has faded by at most a few tenths of a magnitude. Thus the bulge-to-disk ratio increases by a factor of  $\gtrsim 2$  after one gigayear, increasing  $C$  by 0.1 — 0.2 for late-type systems (see Fig.1(b) in Abraham et al [1994]).

To illustrate the impact of this effect upon the radial  $C$  distribution in the cluster, a very simple model was constructed for the morphological composition of a cluster made up of an old component and an infalling field population (whose star formation is truncated by ingress into the cluster). The old component was assumed to be composed of ellipticals and S0s. The infalling field population was assumed to be comprised of 20% ellipticals, 20% S0 galaxies, 20% Sa galaxies, 20% Sb galaxies, and 20% Sc galaxies, which is roughly appropriate for an  $r$ -selected sample (Yee & Green 1987). An even more basic assumption was that the Hubble types could be modeled by the superposition of an exponential disk and a de Vaucouleurs law bulge, with bulge-to-disk ratios for these Hubble types typical of those seen at low redshift. The scale lengths and characteristic surface brightnesses of the disk and bulge components were determined using the relations given in Strom & Strom (1988) and Boroson (1981), assuming that the scale length for the bulge component of spirals follows the canonical relation for ellipticals, as suggested by Kormendy (1985). Differential K-corrections for the bulges and disks were applied using the spectral energy distributions in Coleman, Wu, & Weedman (1980) prior to fading the components.

The fraction of old early type systems (the relics from the initial cluster collapse) varied from 90 percent of the galaxy population in the center of the cluster to 10 percent at 3 Mpc from the cluster core. The disk population was linearly faded as a function of radius, with no fading in the cluster periphery and 1.5 mag fading in the core of the cluster.

Figure 19 shows the morphological data for Abell 2390, binned in radius, with the results from our simple model superposed. The simplistic truncated star-formation model predicts a radial distribution of  $C$  that is in qualitatively good agreement with our morphological data. It therefore appears that the morphological composition of the cluster is consistent with the suggestion from the colors and line indices that the gradients seen in the cluster are the result of an age sequence in an infalling field population whose star formation has been halted by entry into the cluster.

### 7.3. The Butcher-Oemler Effect

It is interesting to consider whether the truncated star formation scenario proposed here may be relevant to galaxy evolution in other rich clusters, as characterized by the Butcher-Oemler effect. In order to determine this, the blue fraction in Abell 2390,  $f_b$ , was measured using the same prescription adopted by Butcher & Oemler (1984) in their classic paper. The number density profile of the cluster was calculated (assuming circular symmetry) and this profile was integrated in order to determine  $R_{30}$ , the radius within which 30 percent of the cluster light was enclosed.  $R_{60}$  and  $R_{20}$  were also calculated in order to determine the cluster concentration parameter  $C_{BO}$ , given by  $C_{BO} = \log R_{60}/R_{20}$ , so that Abell 2390 could be compared to Butcher-Oemler clusters of similar concentration. Colors were normalized to  $r = 19$  mag and transformed to  $B - V$  using Equation 3 in order to reproduce what was done for the B-O clusters. The blue fraction was determined by counting the number of galaxies within  $R_{30}$  that were brighter than  $r = 20$  mag and at least 0.2 mag bluer in  $B - V$  than the locus of the red galaxy population on the color-projected radius diagram. The results from this calculation are shown Table 3, along with data for two Butcher-Oemler clusters, Abell 1942 and Abell 1961, that are similar to Abell 2390 in terms of redshift,  $R_{30}$ ,  $C_{BO}$ , richness, and blue fraction<sup>7</sup>. The overall blue fraction in Abell 2390 is not only very similar to that in Abell 1961 and Abell 1942, it is also in excellent agreement with the canonical  $f_b$  versus  $z$  relation in Butcher & Oemler (1984). The *gradient* in  $f_b$  is also in good agreement with that expected from the Butcher & Oemler (1984) sample at  $z \sim 0.25$ , as shown in Figure 20. However, because of the wide spatial coverage of our present dataset only the inner  $\sim 25\%$  of the Abell 2390 data can be compared to

---

<sup>7</sup>Abell 1942 was observed with the Einstein IPC to have a count rate of 0.015 IPC counts/sec, corresponding to a luminosity  $\sim 5 \times 10^{44}$  ergs<sup>-1</sup>, so its X-ray luminosity is certain to be similar to that of Abell 2390. The X-ray luminosity of Abell 1961 is also likely to be similar, based on the richness-X-ray luminosity correlation in Ebeling et al. (1993), which suggests that the cluster has a luminosity  $> 10^{44}$  ergs<sup>-1</sup>.

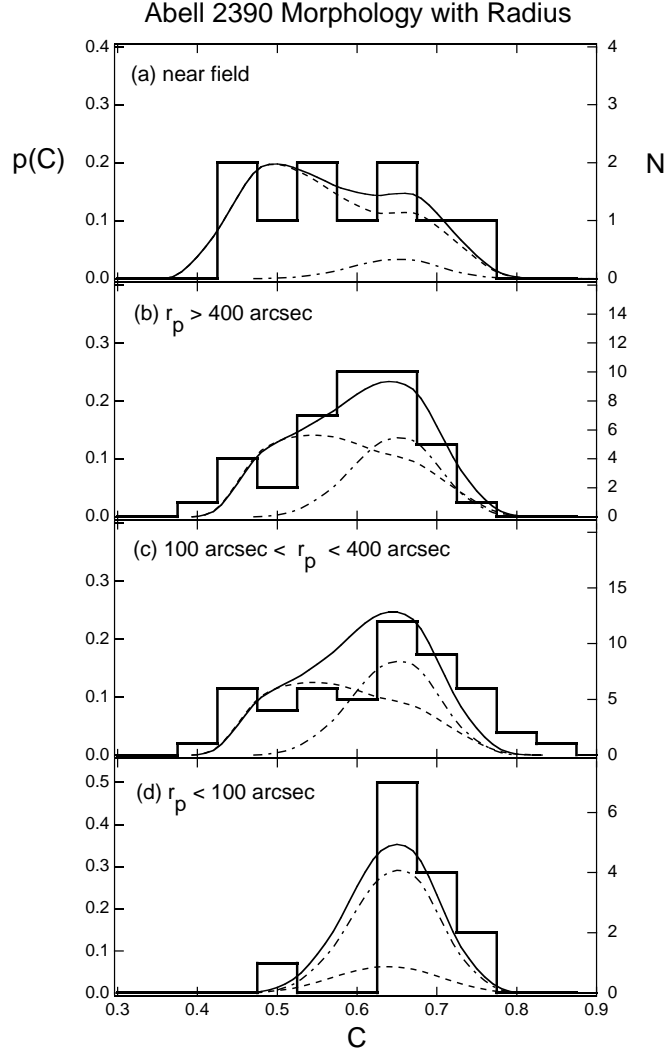


Fig. 19.— Histograms showing the distribution of morphological parameter  $C$ , binned as a function of radius. Superposed are curves corresponding to the simple model described in the text. The solid line is the superposition of the  $C$  distributions for a faded-disk field model (dashed line) and an old elliptical model (dot-dashed line). In the near field bin (a), our models assume that 90 % of the galaxy population is made up of the faded field population (with a disk fading of 0.2 mag), and that the remaining 10% of the galaxies are old ellipticals. In panel (b) we assume disks in the field population have faded by a mean value of 0.5 mag, and that the faded field population comprises 75 percent of the cluster population. In panel (c) we assume a mean fading of 0.7 mag, and that the faded field population comprises 50 percent of the cluster population. In the innermost bin (d), we assume the disks in the field population have faded by 1.5 mag, and that old ellipticals comprise 80 percent of the galaxy population.

the Butcher & Oemler sample. Nevertheless, the similarity between the composition of the galaxy populations in Abell 2390 and typical Butcher-Oemler clusters suggests that the mechanisms driving galaxy evolution in these clusters may be similar.

In order to compare the blue population at large radii in Abell 2390 to samples other than those of Butcher and Oemler, a comparison was made between our data and the Coma sample of Mazure et al. (1988). In Figure 21 we show the differential  $f_b$  in Abell 2390 and Coma as a function of projected radius. In the inner regions of the clusters contamination by blue galaxies from the periphery of the clusters may be occurring, although simulations (and the absence of blue objects near the cluster centers) suggest that such contamination is small, *i.e.* at the level of a few percent. The differential blue fraction of the Abell 2390 is 40% at the periphery of our dataset, compared with the field value of 58%, suggesting that even at large radii red cluster members dominate over blue galaxies. However, at large radii the blue fraction in Abell 2390 is still a factor of two larger than that seen in Coma (Figure 21). The blue fractions in both samples shown in Figure 21 were determined in the same manner, with limiting magnitude cutoffs corresponding to  $r = 21$  mag at  $z = 0.23$ , although both curves remain similar even when the limiting magnitude cutoff is changed by over one magnitude. The size and coverage of the Mazure et al. (1988) sample is quite comparable with the Abell 2390 data set, both samples having some 200 cluster members over a similar range of radius in the cluster rest frame. It is important to note that the Coma colors show no radial gradient analogous to that seen in Abell 2390. However, the slope of the color-magnitude diagram in Abell 2390 is quite similar to that seen in Coma, where  $\delta(B - V)/\delta(B) = 0.027$  (Caldwell 1995, private communication based on analysis of data in Godwin et al. [1983]). Transforming the slope using a elliptical galaxy spectral energy distribution (see §5) gives  $\delta(B - V)/\delta(B) \approx 0.019$  for Abell 2390.

#### 7.4. Cloaked starbursts?

Since there is so little evidence for starbursting activity in Abell 2390, and since four of the five starburst candidates in the cluster and near-field appear to be reddish, it is interesting to consider whether a population of bursting objects may be being cloaked by large amounts of dust. The existence of a population of “cloaked starbursts” could alter the conclusions reached in this paper with regard to the evolutionary history of the cluster population. It is therefore significant that the existence of such a population of “hidden starbursts” can be ruled out on the basis of deep radio observations undertaken with the Very Large Array (VLA). These will be reported in greater detail elsewhere, and will only be outlined here.

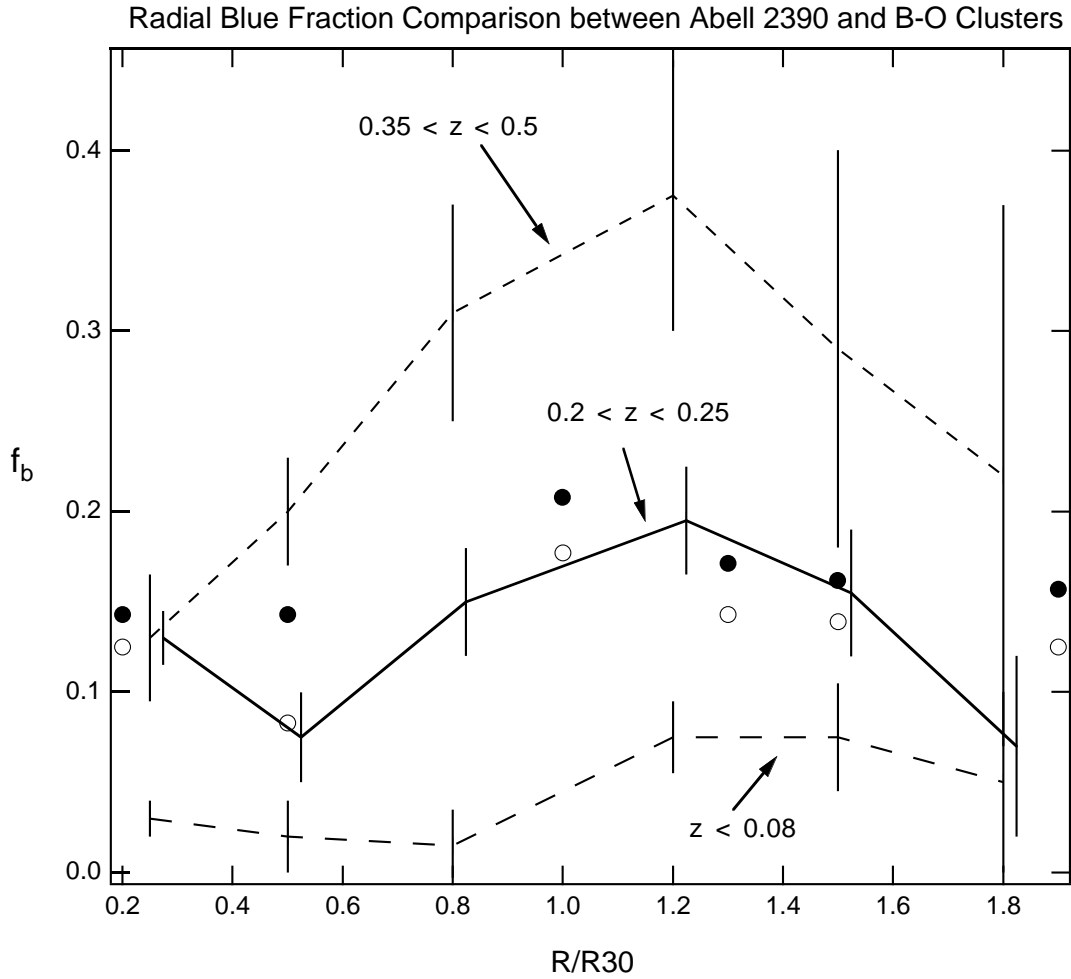


Fig. 20.— A comparison between the radial blue fraction in Abell 2390 (points) and the low redshift (lower dashed line), intermediate redshift (middle dashed line), and high redshift (upper dashed line) samples of Butcher & Oemler (1984). The Abell 2390 data is shown for two limiting magnitudes,  $r < 20.5$  (open circles) and  $r < 20$  (filled circles), in order to demonstrate the low sensitivity of the blue fraction to the choice of limiting magnitude.



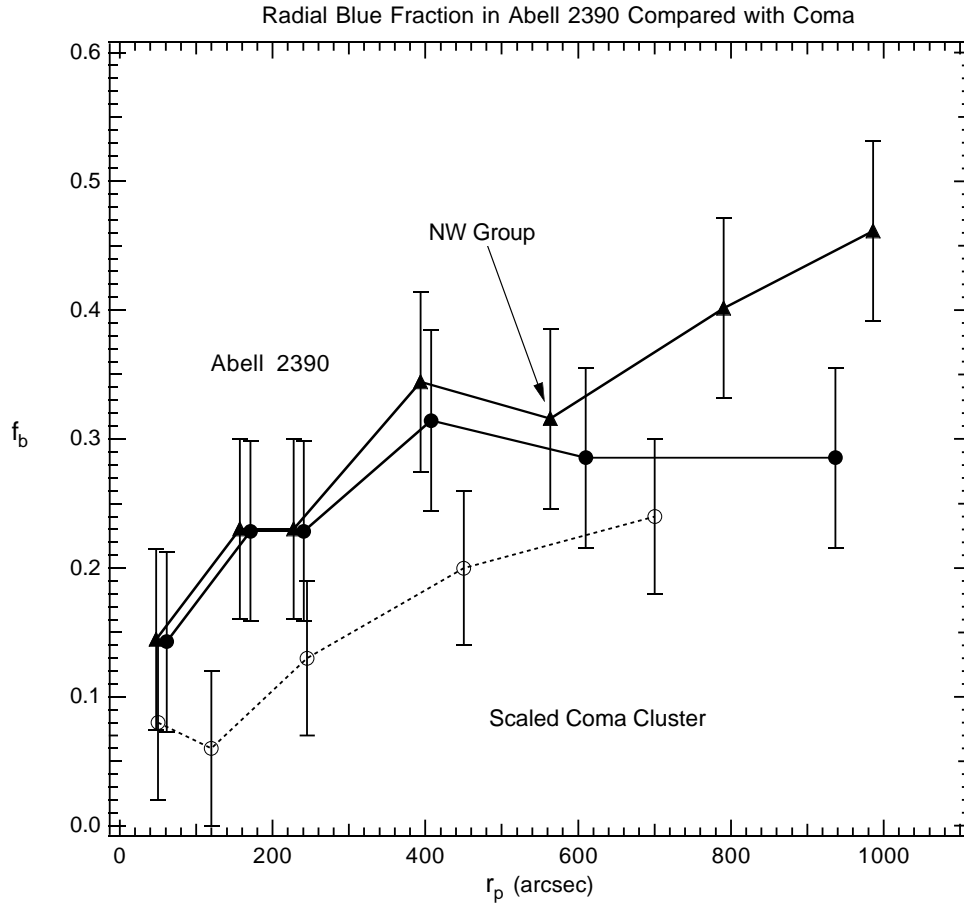


Fig. 21.— A comparison between the differential blue fractions in Abell 2390 and Coma (scaled by a factor of six in radius to account for the distance difference between the two clusters). Each bin in both the Coma and Abell 2390 samples contains 30-40 galaxies. The Coma data are shown by open circles. Abell 2390 points including (filled triangles) and excluding (filled points) the “near-field” galaxies are shown.

VLA maps of Abell 2390 were made with the C-configuration at 6cm and 20cm, covering the optically studied area in three and one pointings, respectively. The limiting detected flux for sources was  $\sim 1$  mJy at 20 cm and 0.3 mJy at 6 cm. These correspond to a (log) power of 22.4 and 22.0 W/Hz at the cluster redshift, typical of a weak Seyfert nucleus or strong star-formation. Thirty two sources were detected at 20 cm and 12 sources at 6 cm, in areas  $\sim 3$  and 0.5 times that of the optically covered fields. Nine of the 12 6 cm sources were detected at 20 cm. The central  $5 \times 5$  arcmin of the cluster contains nine of the sources, indicating a strong central grouping. *Only two (possibly three) of the cluster members in our spectroscopic sample were detected in the radio observations, ruling out the existence of a large population of strongly starbursting objects hidden by dust.* A summary of the properties of the red cluster line-emitters suggests that they are a fairly heterogeneous sample of different types of star-forming galaxies:

**PPP# 101084:** This object is the central cD, and is a strong flat-spectrum point source in the radio with a log power of 24.5 W/Hz. This object has a peculiar spectrum very unlike that of a typical elliptical galaxy, but not atypical for cD galaxies in cooling flow clusters. It has strong emission  $[\text{O II}] = -111 \text{ \AA}$  as well as emission at  $[\text{Ne III}] 3867 = -4.6 \text{ \AA}$ , weak absorption  $\text{H}\delta = 0.9 \text{ \AA}$ , emission at  $\text{H}\gamma = -4.1 \text{ \AA}$  and no detectable G4300 absorption. The emission line spectrum could arise from gas photoionized by young stars, a weak AGN, or from gas cooling in a cooling flow. Our data do not cover the diagnostic  $[\text{O III}]$  or  $\text{H}\alpha$  lines, but Borgne et al. (1991) show this part of the spectrum, and we conclude that the spectrum is a LINER or H II region rather than a Seyfert.

**PPP# 101033:** This object is a marginally detected radio source, and has an equivalent width of  $[\text{O II}] = -52 \text{ \AA}$ , and filled-in Balmer line absorption. Although its projected radius ( $r_p = 78''$ ) is small, it has a high velocity relative to the cluster center, and is likely to be an outer cluster member projected along the line-of-sight to the core of the cluster. The optical appearance of the galaxy is elongated with a low morphological index of  $C = 0.55$ , suggesting that it is a disk system. The galaxy appears to be slightly more extended on one side of the nucleus than the other, possibly due to a recent merger or interaction.

**PPP# 101949:** The spectrum of this object is consistent with a young population and strong Balmer absorption. The optical appearance of this object is very elongated, and the galaxy has a faint companion. The morphological index of this object suggests that it is a late-type system. This galaxy may be a spiral whose colors have been reddened by a dust lane.

**PPP# 500733:** The galaxy appears isolated, but its image lies near the edge of the MOS field of view, and is of poor quality.

### 7.5. The role of mergers and interactions

A major question that has not been addressed in this paper is the role played by tidal events in forming the observed structure and galaxy population of the cluster. Specifically, one would like to know if interactions play an important part in defining the cluster population (*i.e.*, whether or not ellipticals and S0s are forming through mergers), and if so how the merger rate is affected by infall into the cluster. Unfortunately a proper investigation of tidal phenomena in Abell 2390 requires high resolution imaging data, and our current images are not well-suited to this task (due to the comparatively poor resolution, coarse sampling, and variable PSF on our CCD frames). The morphological classifier described in this paper provides much statistical information on galaxy morphologies in Abell 2390, but the nature of the software does not allow the nature of peculiar morphology to be quantified. Future observations and software are planned to address this issue. However, the importance of the morphological evidence and the clear peculiarity of some cluster members leads us to offer the following qualitative remarks based on visual inspection of our images.

The visual inspection was made by one of us (JBH), and was based on an examination of several subsets of the cluster members and near-field galaxies, selected as follows: (a) strong Balmer absorbers ( $H\delta > 4\text{\AA}$ ); (b) strong [O II] emitters ( $>10\text{\AA}$ ,  $3\sigma$ ); (c) galaxies with high limiting isophotes as determined from our automated morphological classifier (a sign of overlapping isophotes, which can be due to crowded fields, peculiar morphology, or image defects); (d) an inactive sample, with no [O II] and weak  $H\delta$  absorption. Another sample, consisting of (e) all field galaxies between  $0.17 < z < 0.37$ , was also examined as a control. The following signs of interaction were looked for: large tidal arms or tails; double nuclei within an asymmetrical envelope; an asymmetrical light distribution about the nucleus; warped disks; or bridges to a companion. Figure 22 shows a montage of images which illustrates these features. The ‘active’ cluster members and field galaxies - (a) and (b) above - have the same fraction ( $\sim 25\%$ ) of objects showing moderate to strong evidence for interactions, compared to the  $< 10\%$  of inactive galaxies - (d) above - which show moderate to strong evidence for interactions. In the field, 18% of the sample showed moderate to strong evidence for interactions. Around 60% of the ‘high isophote’ galaxies have some morphological peculiarity suggesting interaction activity, with the rest being normal but with close companions. Thus, the automated morphological classifier does fairly well at picking interaction candidates. However, most of the high isophote interacting galaxies are not spectroscopically active.

The cluster members and near-field galaxies with [O II] emission were divided into two groups: the seven lying at least  $1\sigma$  above the normal-galaxy region in Figure 17, and the

nine objects lying within the normal galaxy region (to within error bars). Of the high seven, three are probably interacting, two are possibly interacting, and two look quite normal. Of the low nine, none are probably interacting, three are possibly interacting, and six are normal. The number of neighbour galaxies (within  $10''$ ) seen in each group is about the same, averaging about three. Thus, there is a good suggestion that the high [O II] emission may be the result of star-formation triggered by interactions.

In all, 30 galaxies appear to be good interaction candidates, with 40 more being marginal. The spatial distribution of these galaxies roughly follows the density of cluster members, so that they do not obviously occur either at the outside or the inner parts of the cluster. While there are thus definitely *some* interacting galaxies in Abell 2390, the fraction of interacting objects cannot be accurately determined without higher resolution images. The cluster galaxies which are most clearly interacting appear to be red with strong Balmer absorption and no evidence of [O II] emission. It is well-known from the IRAS sample of galaxies that interaction-induced starbursts are often cloaked with dust, and may not be clearly seen at optical wavelengths (e.g., Hutchings & Neff 1991). However, the radio observations described earlier rule out the existence of a population of strongly starbursting systems. Alternatively, these could be mergers of evolved galaxies that contain only small amounts of gas that briefly undergo small bursts of star formation, and hence  $\sim 1$  Gyr after the merger their colors are again dominated by the old stellar component. Quantitative understanding of the role of merging in the cluster population clearly must await better data.

## 8. CONCLUSIONS

Our analysis leads to the following conclusions:

1. Galaxies in the central  $0.4 h^{-1}$  Mpc of Abell 2390 are red and have low dispersions in velocity, color, and spectral line strengths as well as high central concentrations. These properties suggest that they are coeval E/S0 galaxies with ages  $\gtrsim 8$  Gyr (assuming that their star formation timescales are  $\sim 1$  Gyr and that mean metallicities are approximately solar). These objects are likely to be the first generation of galaxies formed in the proto-cluster.

2. Large scale accretion from the field along the West side of the cluster is suggested

Fig. 22.— Montage of R images of the candidate merging/interacting galaxies, centered in each box.

by the spatial-velocity structure of the cluster, and by the the skewed distribution of line emitters (which occur almost exclusively in the West half of the cluster). The most obvious structural subgroup in Abell 2390, the NW Group, may be part of this infall pattern. This group of galaxies is more evolved than its surroundings and is presumably the core of a smaller cluster being accreted onto the main component.

3. Radial gradients exist in the colors, spectral features and morphologies of the cluster galaxies. These radial gradients are interpreted as an age sequence in which the mean age of the galaxies decreases with radius as a consequence of truncated star formation in spirals accreted from the field. Many galaxies in the extensive outer envelope of the cluster have properties intermediate between E/S0s and field spirals. These galaxies are analogous to the “anemic spirals” seen in local clusters (van den Bergh 1976), and they are likely to be transitional objects in an evolutionary sequence in which field spirals are transformed into into cluster S0s. While the blue fraction of the cluster rises strongly as a function of radius, even at the edges of our dataset the galaxy population remains redder than the field.

4. Only  $\lesssim 5\%$  of the galaxies in Abell 2390 show signs of star formation at levels higher than those seen in normal Sbc galaxies. The large number of  $H\delta$  strong objects relative to active galaxies suggests that star formation has been halted in many galaxies, and that in most cases this truncation has occurred in systems that have not undergone starbursts. This suggests that truncation in the star formation rates of cluster members is more closely linked to a gradual mechanism such as stripping by the hot intracluster medium than to starbursts. We cannot rule out the possibility that some ( $\sim 25$ )  $H\delta$ -strong objects are post-starburst systems, but if so then the epoch of cluster starbursts must ended  $\gtrsim 1\text{Gyr}$  before the epoch of observation.

5. The blue fraction in Abell 2390 is typical of that seen in “Butcher-Oemler” clusters at  $z \sim 0.25$ . The recent HST results of Couch et al. 1994 and Dressler et al. 1994 suggest that the increased blue fraction in high-redshift clusters is due to a high proportion of blue disk galaxies. If Abell 2390 is really a “typical” rich cluster at intermediate redshift, then truncated star formation leading to the transformation of the blue disks in high redshift clusters may be the physical mechanism driving the Butcher-Oemler effect. Future papers will compare Abell 2390 to other CNOC clusters (which span the redshift range  $0.2 \leq z \leq 0.5$ ) in order to determine whether similar mechanisms are driving galaxy evolution in other X-ray luminous clusters.

#### Acknowledgments

The data used in this paper forms part of the CNOC (Canadian Network for Observational Cosmology) study of intermediate redshift clusters. We are grateful to all

the consortium members, and to the CFHT staff (particularly Telescope Operators Ken Barton, John Hamilton, and Norman Purves) for their contributions to this project. We also thank Sidney van den Bergh, Richard Ellis, and Alastair Edge for useful discussions.

## REFERENCES

- Abraham, R. G., Valdes, F., Yee, H. K. C., & van den Bergh, S. 1994, *ApJ*, 432, 75
- Aragón-Salamanca, A., Ellis, R. S., Couch, W. J., & Carter, D. 1993, *MNRAS*, 262, 764
- Beers, T., Geller, M. J., & Huchra, J. P. 1982, *ApJ*, 257, 23
- Bohlin, R. C., Jenkins, E. B., Spitzer, L. J., York, D. G., Hill, J. K, Savage, B. D., & Snow, T. P. J. 1983, *ApJ Supp*, 51, 277
- Borgne, J. Le, Mathez, G., Mellier, Y., Pello, R., & Sanahuja, B. 1991, *AA*, 88, 133
- Boroson, T. 1981, *ApJ Supp*, 46, 177
- Bressan, A., Chiosi, C., & Fagotto, F. 1994, *ApJ Supp*, 94, 63
- Bruzual, G. & Charlot, S. 1993, *ApJ*, 405, 538
- Burstein, D. & Heiles, C. 1982, *AJ*, 87, 1165
- Butcher, H. & Oemler, A. 1984, *ApJ*, 285, 426
- Carlberg, R., Yee, H. K. C., Ellingson, E., Abraham, R., Gravel, P., Morris, S., & Pritchett, C. 1995, Submitted to *ApJ*
- Carlberg, R. G., et al. 1994, *JRASC*, 88, 39
- Charlot, S. & Silk, J. 1994, *ApJl*, 432, 543
- Coleman, G. D., Wu, C.-C., & Weedman, D. W. 1980, *ApJSupp*, 43, 393
- Couch, W. J., Ellis, R. S., Sharples, R. M., & Smail, I. 1994, *ApJ*, 430, 121
- Couch, W. J. & Sharples, R. M. 1987, *MNRAS*, 229, 423
- Cowie, L. L. & Songaila, A. 1977, *Nature*, 266, 501
- Davidge, T. & Clarke, C. C. 1994, *AJ*, 107, 946

- Doi, M., Fukugita, M., & Okamura, S. 1993, MNRAS, 264, 832
- Dressler, A. 1980, ApJ, 236, 351
- Dressler, A. & Gunn, J. E. 1982, ApJ, 263, 533
- Dressler, A. & Gunn, J. E. 1983, ApJ, 270, 7
- Dressler, A., Oemler, A., Butcher, H. R., & Gunn, J. E. 1994, ApJ, 430, 107
- Dressler, A. & Shectman, S. A. 1987, AJ, 94, 899
- Ebeling, H., Voges, W., Böhringer, H., & Edge, A. C. 1993, AA, 275, 360
- Efstathiou, G., Ellis, R. S., & Peterson, B. A. 1988, MNRAS, 232, 431
- Gunn, J. E. & Gott, J. R. 1972, AJ, 176, 1
- Hamilton, D. 1985, ApJ, 297, 371
- Haynes, M. P. 1988, in “The Minnesota Lectures on Clusters of Galaxies and Large Scale Structure” ASP Conference Series
- Hutchings, J. B. & Neff, S. G. 1991, AJ, 101, 434
- Kennicutt, R. C. 1992, ApJ Supp, 79, 255
- Kent, S. M. 1985, AJ, 97, 165
- Kimble, R. A., Davidsen, A. F., & Sandage, A. R. 1989, A&A Supp, 157, 237
- Koo, D. 1988, In “Towards Understanding Galaxies at Large Redshift”, eds. R. G. Kron & A. Renzini,, 275
- Kormendy, J. 1985, ApJ, 295, 73
- Le Fevre, O., Crampton, D., Fellenbok, P., & Monet, G. 1993, AA, 282, 325
- Lynden-Bell, D. 1967, MNRAS, 136, 101
- Mazure, A., Proust, D., Mathez, G., & Mellier, Y. 1988, A&A Supp, 76, 339
- McMillan, S. L. W., Kowalski, M. P., & Ulmer, M. P. 1989, ApJSupp, 70, 723
- Morgan, W. W. 1958, PASP, 70, 364
- Quinn, P. J., Salmon, J., & Zurek, W. H. 1986, Nature, 322, 329

- Regős, E. & Geller, M. J. 1989, *AJ*, 98, 755
- Scalo, J. M. 1986, *Fundamentals of Cosmic Physics*, 11, 1
- Shapley, H. 1927, *Harvard. Obs. Bull.*, 846, 1
- Solanes, J. M., Salvador-Solé, E., & Sanromà, M. 1989, *AJ*, 98, 798
- Strom, S. E. & Strom, K. M. 1988, *AJ*, 83, 732
- Valdes, F. 1982, In *SPIE, Instrumentation in Astronomy*, IV, 465
- van den Bergh, S. 1976, *ApJ*, 206, 883
- West, M. J. & Bothun, G. D. 1990, *ApJ*, 353, 344
- Worthey, G. 1994, *ApJ Supp*, 95, 107
- Yee, H. K. C., Ellingson, E., Abraham, R. G., Gravel, P., Carlberg, R., Smecker-Hane, T., Schade, D., & Rigler, M. A. 1996, Accepted for publication in *ApJ Supp*.
- Yee, H. K. C., Ellingson, E., & Carlberg, R. 1996, Accepted for publication in *ApJ Supp*.
- Yee, H. K. C. & Green, R. F. 1987, *AJ*, 94, 618
- Yee, H. K. C., Sawicki, M., Ellingson, E., & Carlberg, R. 1995, in “Fresh View of Elliptical Galaxies” *ASP Conference Series*